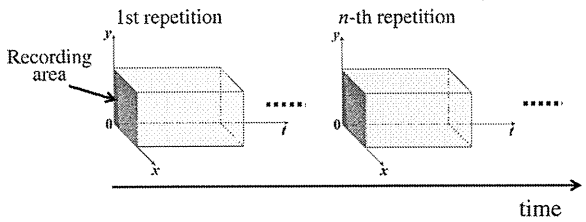

Fig. 5. Conceptual representation of the structure of the optical imaging data. The recorded imaging data can be reconstructed with three-dimensional data (two-dimensional space corresponding to recording area and time axis) for each repetition.

identified model and the innovations were estimated. We defined the origin of time axis as the onset of respiratory activity observed in the C4VR signal. The NNAR model was identified on the period sufficiently before the onset of respiratory activity, i.e., from −4.22 to −2.24 s (100 time frames). Subsequently, the period from −2.22 to 5.24 s (374 time frames) was filtered for the data1.

In order to investigate basic oscillatory properties of the data, we computed power spectrum using standard fast Fourier transformation (FFT). Fig. 6(c) shows averaged power spectrum across all pixels and all repetitions of imaging data and innovations. There were three major peaks in the power spectrum of the imaging data, which corresponded to about 0.1–0.5 Hz, 3.0–6.0 Hz, and 12.0–14.0 Hz, respectively. Spatial distribution map corresponding to these peaks are represented in Fig. 6(a). The spatial distribution pattern for 0.1–0.5 Hz nearly corresponded to the reported respiratory-related regions [2]. On the other hand, the latter two could correspond to stationary background oscillation originating from mechanical vibration of the recording system and/or turbulence associated with circulation of the perfusion fluid. Through this fundamental analysis, the respiratory activities appeared at a very low frequency of 0.1–0.5 Hz, whereas stationary background oscillations were seen at 3.0–6.0 Hz and 12.0–14.0 Hz ranges. In contrast, the peaks corresponding to the back ground oscillations significantly diminished in the power spectrum of innovations [Fig. 6(a)]. Moreover, spatial distribution maps were nearly homogenous, and any characteristic structure could not be observed, suggesting that the background stationary oscillations were accurately identified by the NNAR model and removed from the innovations. Because of the difference in the amplitude of imaging data and innovations, the intensity of power spectrum cannot be directly compared (the amplitude of innovations are smaller than imaging data). Therefore, the power spectrums were normalized.

In principle, model order of the NNAR model should be optimized according to some criterion, such as, Akaike information criterion (AIC) [14] for each pixel. However, since it would not be appropriate to individually optimize the model order for a large number of pixels, a common value should be chosen. It is important to choose a sufficiently large value, lest any relevant correlations in the data should be missed. On the other hand, too large model orders may cause over-fitting problems and reduce the reliability of the estimated model parameter values. In this study, the model order for p and q in (6) was fixed to the same values for the simplification of the model. We gradually

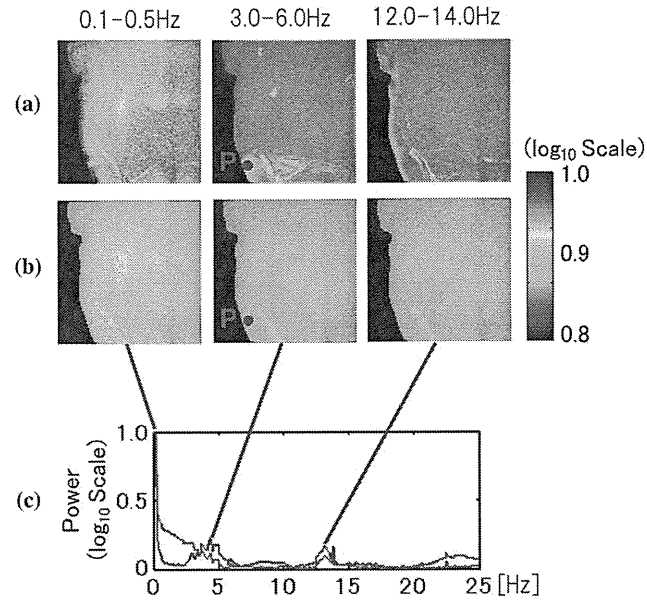

Fig. 6. Spatial distribution of averaged power spectrum in a limited frequency band for the optical recording data (a) and innovations (b). (c) Normalized averaged spectral power across all pixels and all repetitions for the optical recording data (blue line) and innovations (red line). The pixel on the point P is located in the region that was maximally contaminated with the background oscillation at 3.0–6.0 Hz. The raw imaging data and innovations correspond to this point and its eight neighbored pixels were used for further autocorrelation analysis.

increased the model order from two and found that stationary oscillations were properly identified and removed from the innovation by NNAR model with $p = q = 7$. Therefore we conclude that for our data a model order of this value represents a good compromise.

We further investigated whether the temporal correlation caused by background oscillation in the time series could be removed by NNAR model. The pixel at the point P in Fig. 6 is located in the region that was maximally contaminated with background oscillation at 3.0–6.0 Hz, and we selected this point as an example under severe condition. The autocorrelation functions of raw imaging data and innovations at the point P and its eight neighbored pixels were computed. Although autocorrelation functions of the imaging data contain strong temporal correlations at 4.0–5.0 Hz, the autocorrelation functions of innovations do not show any notable correlation (Fig. 7). These results indicate that the NNAR model could successfully reduce serial correlation from the imaging data.

We evaluated the statistical significance of the difference of mean amplitude of the innovations in the period of model identification and filter output by the method mentioned in Fig. 3. This procedure was repeated for all pixels, and then temporal transition of activation t-map was illustrated. Five representative time frames of activation time map are illustrated as time dependent t-maps in Fig. 8(c), which shows the area and time at which significant dynamic state transition arises. The activation initiated at the caudal part of pFRG, corresponding to the rostral ventrolateral medulla (RVLM) [12] and [15], and then extended rostrally toward the rostral part of pFRG and caudally toward the preBötC. Subsequently the activation traveled to more caudal structures of the brain. Finally the activation of the high cervical spinal cord reached its maximum (Fig. 8(c) in

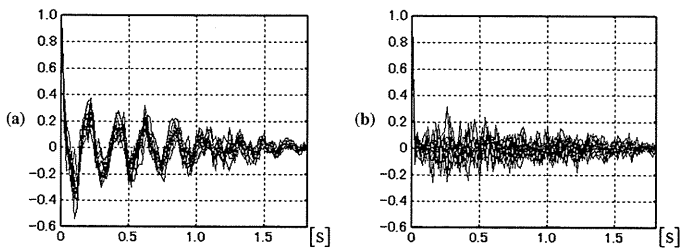

Fig. 7. Multiple plots of autocorrelation functions for raw imaging data (a) and innovations (b) corresponding to the pixel P in Fig. 6 and eight neighboring pixels. The signals of raw imaging data and innovations were z-transformed. The raw imaging data are contaminated with strong background oscillation at 4.0–5.0 Hz. On the contrary, any notable temporal correlation does not remain in the innovations, which are filter output of NNAR model.

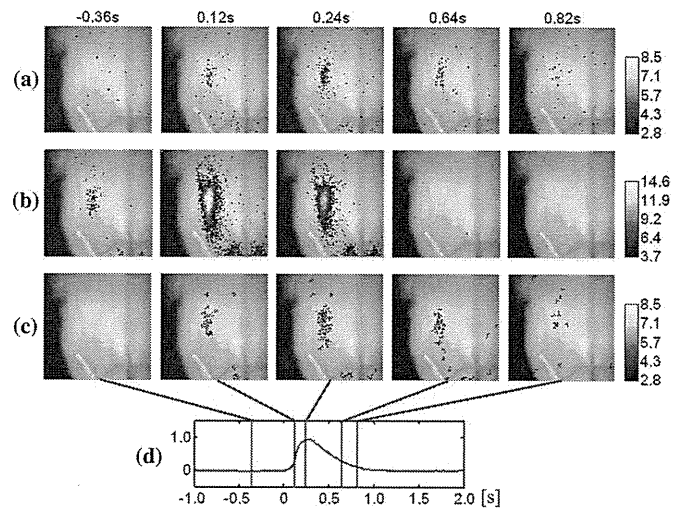

Fig. 8. Representative time frames of temporal transition of the activation t-maps for the imaging data (a) and the innovations (c), and the correlation t-map with averaged imaging data across repetition (b). The C4VR output signal and time points corresponding to the time frames (d). The t-maps were thresholded of $p < 0.05$ [corrected by the false discovery rate (FDR)] and a cluster extent of five pixels.

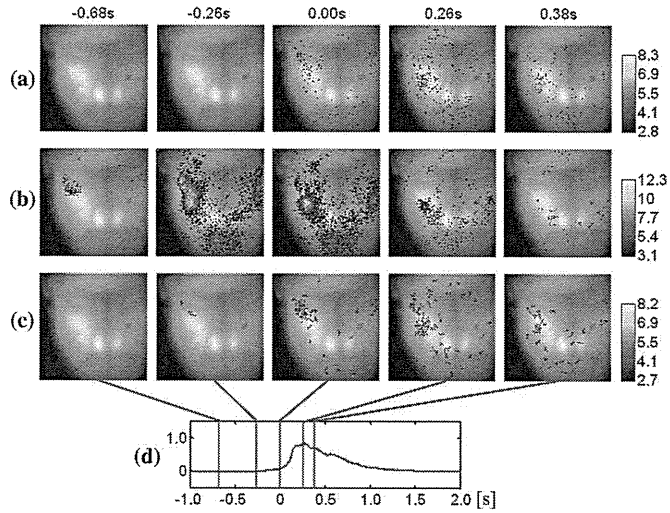

Fig. 9. Representative time frames of temporal transition of the activation t-maps for the imaging data (a) and the innovations (c), and the correlation t-map with averaged imaging data across repetition (b). The C4VR output signal and time points corresponding to the time frames (d). The t-maps were thresholded of $p < 0.05$ (corrected by the FDR) and a cluster extent of five pixels.

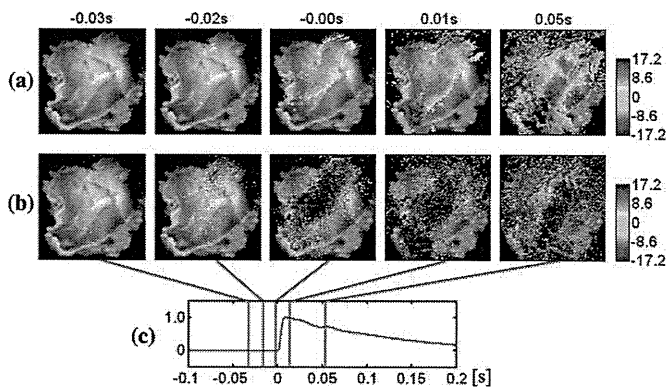

Fig. 10. Representative time frames of temporal transition of the activation t-maps for the imaging data from the rabbit cardiac sino-atrial node (SAN) (a) and the innovations (b). The C4VR output signal and time points corresponding to the time frames (d). The t-maps were thresholded of $p < 0.05$ (corrected by the FDR) and a cluster extent of five pixels.

the time frame at 0.24 s) just before the peak of C4VR output signals [Fig. 8(d)]. Further, a line from preBötC toward caudal brain structures could be seen in Fig. 8(c) in the time frame at 0.64 s. This sequence may correspond to the fact that caudal brain structures such as ventral respiratory group (VRG) contain premotor and motor neurons that relay respiratory outputs to the C3-5 segments of the spinal cord with a certain time delay.

Fig. 8(a) displays activation t-maps for the raw imaging data instead of the innovations using the procedure described above. Although both images for the imaging data and innovations were thresholded at the same level, significant areas for the imaging data were less than those for the innovations. Further, the propagation from the preBötC toward caudal brain structures could not be detected in activation t-maps for the raw imaging data.

The results of correlation analysis with averaged imaging data across repetitions are illustrated in Fig. 8(b) as correlation t-maps. The respiratory related activated areas, such as pFRG and preBötC, were effectively detected. However, the duration of detected activations was shorter than that of activation t-maps for the innovations. Besides, the propagation from the preBötC toward caudal brain structures could not be detected.

Data2 did not have enough time frames before the onset of respiratory activation because of the parameter setting for setting recording condition. Therefore the analysis cannot be applied to data2 under the same condition for data1. In order to solve this problem, the NNAR model was identified at the period sufficiently after the offset of respiration, i.e., from 1.98 to 3.96 s (100 time frames), and then the period from −1.12 to 1.96 s (155 time frames) was filtered. The activation t-maps for the imaging data and innovations are illustrated in Fig. 9(a) and (c), respectively. The correlation map is shown in Fig. 9(b). The analyses yielded similar results to those for data1. Furthermore, the time lag of the activation between preBötC and VRG could be clearly detected in the activation time map for the innovations (Fig. 9(c) in the time frames of 0 s and 0.26 s), which was not distinct in the correlation map [Fig. 9(b)].

We attempted to apply our method to other type of data, i.e., voltage imaging data of the SAN, in order to evaluate the performance of our method. The recorded electrical field potential of the SAN may be employed as the reference function for cross correlation analysis. However, the imaging data after the peak were contaminated with heavy artifact and the tissue was deviated from its original positions because of periodic contraction of the SAN. Therefore the cross correlation analysis was not appropriate for the imaging data of SAN.

On the contrary, our method was applicable, even though there was an artifact contamination in some temporal region. The NNAR model was estimated on the period sufficiently before the onset of action potential, from -0.23 s to -0.114 s (59 time frames), and then the period from -0.112 s–0.466 s (290 time frames) was filtered.

Fig. 10 shows activation t-maps for raw imaging data and innovations. Although the maps were thresholded with the same level, detected activation areas for the innovations were larger than those for the imaging data. Moreover, the beginning of the activation was sensitively detected for the innovations (in the time frame at -0.03 s). The propagation of action potential could be observed. The regions with negative t-values in the time frame at 0.05 s corresponded to the trough caused by the contraction artifact.

V. Discussion

Using the ordinary cross correlation analysis, which is equivalent to the time-lagged cross correlation analysis with a restriction $\tau = 0$, only one of the two respiratory rhythm generators, the preBötC, was detected with data2. The result can be seen in Fig. 9(b) in the time frame at 0.00 s. The reason why the other respiratory rhythm generator pFRG was missed is that the activation of pFRG appeared earlier than the onset of the C4VR activity in the reference function. Therefore significant correlation was not found between pFRG and C4VR signals. In this situation, time-lagged cross correlation analysis gave a solution. Oku, *et al.* [2] applied this method to the optical imaging data and reported an earlier respiratory activation in the pFRG [Fig. 9(b)].

However, there are still several problems remain in the ordinary or time-lagged cross correlation analysis. First, it does not consider dynamical properties of time series, but evaluates only morphological resemblance between two time series. Therefore only pixels whose temporal activity pattern has a similar shape to the reference function can be detected. Second, it has been applied only to averaged imaging data across the repetition of means. Any method has not been proposed that can be applied to each repetition nor statistically evaluated across the repetition of the measurement. Third, in the case of the time-lagged correlation analysis, the larger the time lag is, the shorter the overlapping length of the two time series becomes. Then, inaccuracy of the analysis will increase with larger time lags. Fourth, the absolute time point of the appearance of activations cannot be investigated by time-lagged cross correlation analysis. This is because the origin of time axis is defined arbitrarily. Therefore the correlation t-map of averaged imaging data and activation t-map for innovations cannot be compared on the common time axis. If the time point corresponding to the peak of C4VR signal is selected as the origin of time frame for the time-lagged cross correlation, the time point of the onset of activations in the correlation t-map and activation t-map will agree.

Our method is free from the above-mentioned problems. Namely, our method can sensitively detect the spatio-temporal emergence of activations through the investigation of the dynamic state transition and statistical evaluation across the repetition of the measurement. The earliest activation is localized in RVLM (the caudal part of pFRG), which can be seen typically with data2 (Fig. 9(c) in the time frame at -0.26 s). The activation extends bidirectionally to the rostral part of pFRG and to the preBötC region and travels to the high cervical spinal cord (Fig. 8(c) in the time frame at 0.64 s, and Fig. 9(c) in the time frame at 0.26 s). In the case of imaging data of SAN, the onset of activation could be detected by our method at least 0.01 s earlier than the result from the analysis using imaging data instead of innovations (Fig. 10(b) in the time frame at -0.03 s).

In this study, we analyzed the data that were recorded with multiple repetitions. Fig. 3 shows the temporal transition of the amplitude of innovations that was estimated in the simulated data. In the case of the data with single repetition, the line B will consist of only one innovation. Therefore, mean amplitudes of the innovations in the area A and on the line B cannot be statistically evaluated because of the insufficient number of samples. Nevertheless, our method is applicable if the line B is replaced with a time window in order to obtain sufficient number of samples, i.e., innovations, although there is a trade-off with respect to temporal resolution.

In order to estimate a neuronal network system, several methods, e.g., correlation analysis and Akaike causality [16], have been used. Whichever method is chosen, if it is directly applied to imaging data, a huge number of combinations of pixels have to be considered. This is not realistic, even though it could be done. Therefore, another procedure to extract a functional network structure from the imaging data is necessary. In order to avoid these problems, the regions of interest (ROIs) to estimate the network need to be set by preliminary analysis. In our method, the detected regions, where dynamic state transitions arose, may have spatial dynamic correlation associated with anatomical connections and play substantial roles to form a functional network structure. Namely, our method serves as a new approach to define ROIs and estimate functional network structures consistently.

We conclude that our method can precisely detect the biological activation without employing additional information such as reference time series data, and the significance can be evaluated with statistical test values. Further, it can be generally used to spatio-temporal data, e.g., fMRI, electroencephalography, near infrared spectroscopy.

References

[1] K. J. Friston, A. P. Holmes, K. J. Worsley, J. B. Poline, C. D. Frith, and R. S. J. Frackowiak, "Statistical parametric maps in functional imaging: A general linear approach," *Hum. Brain. Mapp.*, vol. 2, no. 4, pp. 189–210, 1995.

[2] Y. Oku, H. Masumiya, and Y. Okada, "Postnatal developmental changes in activation profiles of the respiratory neuronal network in the rat ventral medulla," *J. Physiol.*, vol. 585, no. 1, pp. 175–186, 2007.

[3] Y. Oku, N. Kimura, H. Masumiya, and Y. Okada, "Spatiotemporal organization of frog respiratory neurons visualized on the ventral medullary surface," *Respir. Physiol. Neurobiol.*, vol. 161, no. 3, pp. 281–290, 2008.

[4] Y. Okada, H. Masumiya, Y. Tamura, and Y. Oku, "Respiratory and metabolic acidosis differentially affect the respiratory neuronal network in the ventral medulla of neonatal rats," *Eur. J. Neurosci.*, vol. 26, no. 10, pp. 2834–2843, 2007.

[5] H. Masumiya H, Y. Oku, and Y. Okada, "Inhomogeneous distribution of action potential characteristics in the rabbit sino-atrial node revealed by voltage imaging," *J. Physiol. Sci.*, vol. 59, no. 3, pp. 227–241, 2009.

[6] T. Kailath, "An innovation approach to least-square estimation Part I: Linear filtering in additive white noise," *IEEE Trans. Automat. Control*, vol. 13, no. 6, pp. 646–655, Dec. 1968.

[7] T. Kailath, "An innovation approach to least-square estimation Part II: Linear smoothing in additive noise," *IEEE Trans. Automat. Control*, vol. 13, no. 6, pp. 655–660, Dec. 1968.

[8] H. Kato and T. Ozaki, "Adding data process feedback to the nonlinear autoregressive model," *Signal Process.*, vol. 82, no. 9, pp. 1189–1204, 2002.

[9] J. C. Jimenez and T. Ozaki, "An approximate innovation method for the estimation of diffusion processes from discrete data," *J. Time Ser. Anal.*, vol. 27, no. 1, pp. 77–97, 2006.

[10] A. Galka, T. Ozaki, J. B. Bayard, and O. Yamashita, "Whitening as a tool for estimating mutual information in spatiotemporal data sets," *J. Stat. Phys.*, vol. 124, no. 5, pp. 1275–1315, 2006.

[11] K. Katanoda, Y. Matsuda, and M. Sugishita, "A spatio-temporal regression model for the analysis of functional MRI data," *Neuroimage*, vol. 17, no. 3, pp. 1415–1428, 2002.

[12] H. Onimaru and I. Homma I, "A novel functional neuron group for respiratory rhythm generation in the ventral medulla," *J. Neurosci.*, vol. 23, no. 4, pp. 1478–1486, 2003.

[13] J. C. Smith, H. H. Ellenberger, K. Ballanyi, D. W. Richter, and J. L. Feldman, "Pre-Botzinger complex: A brainstem region that may generate respiratory rhythm in mammals," *Science*, vol. 254, no. 5032, pp. 726–729, 1991.

[14] H. Akaike, "A new look at the statistical model identification," *IEEE Trans. Automat. Contr.*, vol. 19, no. 6, pp. 716–723, 1974.

[15] H. Onimaru, A. Arata, and I. Homma, "Primary respiratory rhythm generator in the medulla of brainstem-spinal cord preparation from newborn rat," *Brain Res.*, vol. 445, no. 2, pp. 314–324, 1988.

[16] H. Akaike, "On the use of a linear model for the identification of feedback systems," *Ann. Inst. Stat. Math.*, vol. 20, no. 3, pp. 425–439, 1968.

Respiratory Physiology & Neurobiology 177 (2011) 207–211

Contents lists available at ScienceDirect

Respiratory Physiology & Neurobiology

journal homepage: www.elsevier.com/locate/resphysiol

Short communication

A μ-opioid receptor agonist DAMGO induces rapid breathing in the arterially perfused *in situ* preparation of rat

Tadachika Koganezawa[a], Yasumasa Okada[b], Naohito Terui[a], Julian F.R. Paton[c], Yoshitaka Oku[d,*]

[a] Department of Physiology, Institute of Basic Medical Sciences, Graduate School of Comprehensive Human Sciences, University of Tsukuba, Tsukuba 305-8575, Japan
[b] Department of Medicine, Keio University Tsukigase Rehabilitation Center, Shizuoka 410-3215, Japan
[c] School of Physiology and Pharmacology, Bristol Heart Institute, Medical Sciences Building, University of Bristol, Bristol BS8 1TD, UK
[d] Department of Physiology, Hyogo College of Medicine, Nishinomiya, Hyogo 663-8501, Japan

ARTICLE INFO

Article history:
Accepted 5 April 2011

Keywords:
DAMGO
Respiration
Central pattern generator
Vagus nerve

ABSTRACT

Ventilatory responses to opioids are complex and not yet fully understood. We evaluated concentration-dependent effects of a selective μ-opioid receptor agonist [D-Ala(2),N-Me-Phe(4),Gly(5)-ol]-enkephalin (DAMGO) on respiratory output in the arterially perfused *in situ* rat preparation, which preserves the integrity of the ponto-medullary respiratory network. DAMGO (300–3400 nM) was added accumulatively to the perfusate. DAMGO increased inspiratory time and diminished central vagal post-inspiratory activity. At 300–500 nM DAMGO caused rapid breathing with shortening of expiratory time. The change of breathing pattern occurred within a single breath. Bilateral vagotomy did not affect the change in respiratory pattern, suggesting that it was of central origin. Additional DAMGO up to 1800 nM did not affect the rapid breathing pattern, and further elevated concentrations (up to 3400 nM) caused inconsistent results. Since the rapid breathing pattern was associated with the obliteration of vagal post-inspiratory activity, we conclude that DAMGO reconfigures the respiratory output to an inspiratory phase-dominant, rapidly alternating inspiration–expiration pattern.

1. Introduction

Ventilatory depression by opioids was recognized in the 14th century. Respiratory complications of opioids include depression of respiratory rate, tidal volume, and sensitivity to CO_2 and hypoxia (Hickey and Severinghaus, 1981). Although substantial efforts have been made to understand opioid effects on respiratory control, mechanisms of ventilatory responses to opioids remain unclear. Intravenous administration of a μ-opioid receptor agonist, remifentanyl, depresses bulbospinal respiratory premotor neurons in dogs (Stucke et al., 2008). However, local picoinjection of naloxone onto bulbospinal premotor neurons does not reverse the depression, regardless of the opioid receptor types (μ, δ_1, or δ_2) expressed in these neurons (Stucke et al., 2008). These findings suggest that opioid-induced effects are on neurons antecedent to these premotor neurons.

In neonatal *in vitro* rodent preparations, a selective μ-opioid receptor agonist [D-Ala(2),N-Me-Phe(4),Gly(5)-ol]-enkephalin (DAMGO) slows respiratory rhythm (Mellen et al., 2003), which is considered to be due to the depressant effect of DAMGO on the pre-Bötzinger complex (preBötC), a medullary region essential for respiratory rhythmogenesis (Smith et al., 2007). In *in vitro* brainstem spinal cord preparations, respiratory periods lengthen non-deterministically to integer (actually fractional) multiples of the control period, which is termed quantal slowing (Mellen et al., 2003). However, DAMGO injection into the preBötC and its surrounding region in awake adult goats does not alter eupneic breathing (Krause et al., 2009), suggesting that in awake mammals respiratory depression by opioids is not due to their direct action on preBötC neurons. Since μ-opioid receptors are abundantly expressed in respiratory-related areas in the pons (Chamberlin et al., 1999) and the medulla (Lonergan et al., 2003; Manzke et al., 2010), and the respiratory pattern generation is dependent on these dispersed neuronal areas in intact adult animals (Smith et al., 2007), the depression of preBötC neurons may have less influence on the respiratory rhythm than when applied to reduced circuitry or tissue in which only a part (e.g., preBötC) is functional. Further, Czapla et al. (2000) reported that intravenous injection of DAMGO *in vivo* decreases ventilation at a low concentration, but increases ventilation at a high concentration. This is in contrast with the ventilatory response to the intravenous injection of morphine, which is the consistent decrease in ventilation at any concentration (Czapla et al., 2000). Differences in ventilatory responses to these μ-opioids may be due to distinct pharmacological characteristics, e.g., different potency for G_α protein subtypes (Saidak et al., 2006). To further understand the effects of μ-opioid agonists on breath-

* Corresponding author. Tel.: +81 798 456 387; fax: +81 798 489 643.
E-mail address: yoku@hyo-med.ac.jp (Y. Oku).

1569-9048/$ – see front matter © 2011 Elsevier B.V. All rights reserved.
doi:10.1016/j.resp.2011.04.002

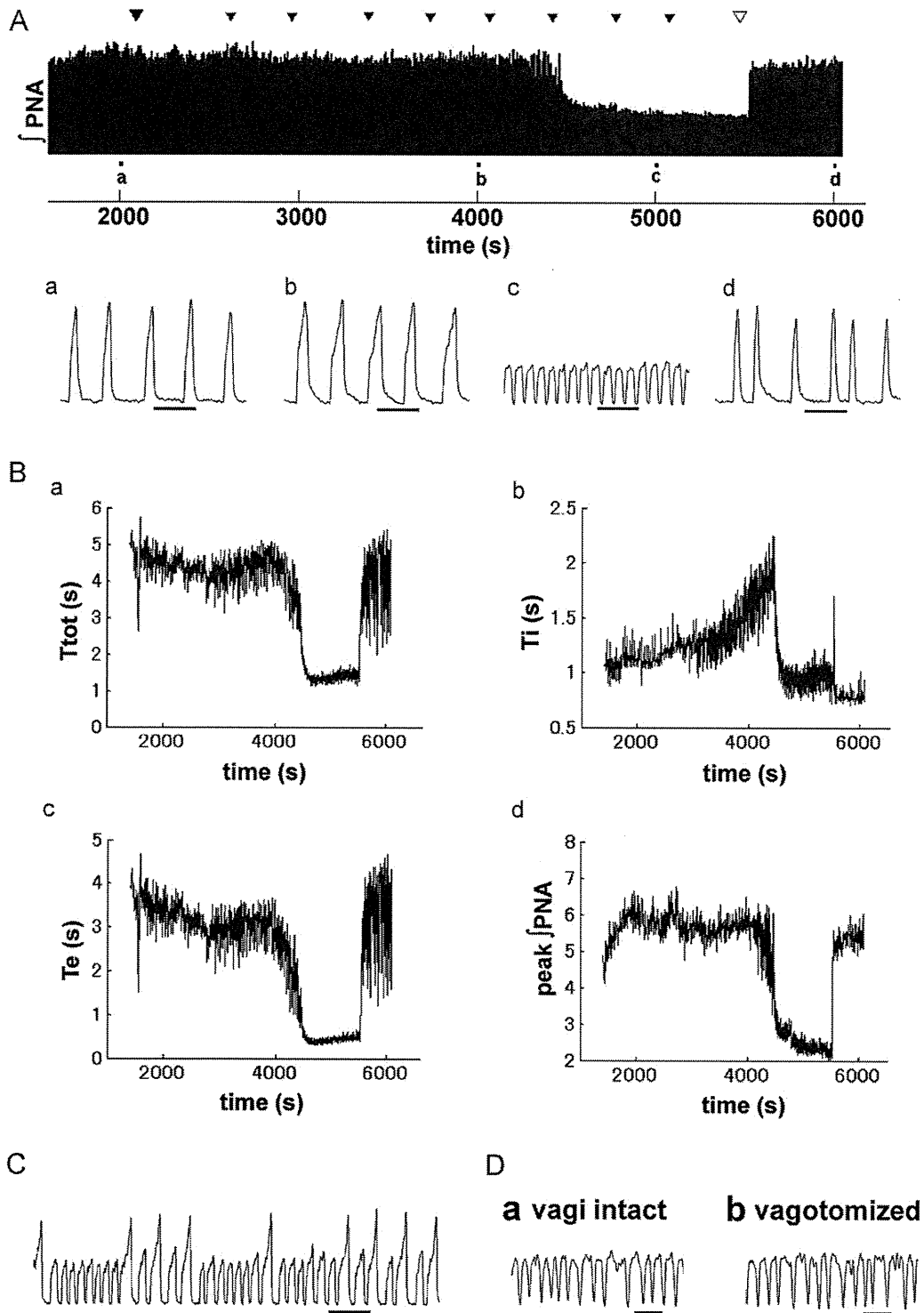

Fig. 1. Effects of DAMGO on the integrated phrenic activity in the arterially perfused *in situ* preparation. (A) A representative trace of the integrated phrenic nerve activity (∫ PNA) is shown. 200 nM DAMGO was initially applied to the perfusate (large filled arrowhead). Subsequently the DAMGO concentration was increased by 50 nM every 5–10 min (indicated by small filled arrowheads). Finally, 10 μM naloxone was added to the perfusate (open arrowhead). Aa–Ad show enlarged traces at periods indicated below the overview trace. (B) Ba–Bd show time courses of T_{tot}, T_i, T_e, and the amplitude of the integrated phrenic activity (peak ∫PNA), respectively, over the same time period shown in (A). Inspiratory time was prolonged after application of DAMGO before a sudden change to rapid breathing with extremely shortened T_e. Naloxone (10 μM) completely reversed these changes in breathing pattern. However, variation in respiratory cycle time persisted. Bars in Aa–Ad, 5 s. (C) An example where eupnea and rapid breathing occurred interchangeably observed during the transition between eupneic and rapid breathing patterns. Bar, 10 s. (D) Vagotomy did not change the rapid breathing pattern. Bars in Da–Db, 5 s.

ing, we explored concentration-dependent effects of DAMGO in the arterially perfused *in situ* rat preparation (Paton, 1996), which preserves the integrity of the ponto-medullary respiratory network generating a 3-phase pattern, is decerebrated and free from the confounding effects of anesthesia, and allows studies in an *in vitro* milieu. Here, we tested the hypothesis that DAMGO would depress a component(s) of the 3-phase respiratory pattern. We report that post-inspiration was most susceptible to DAMGO.

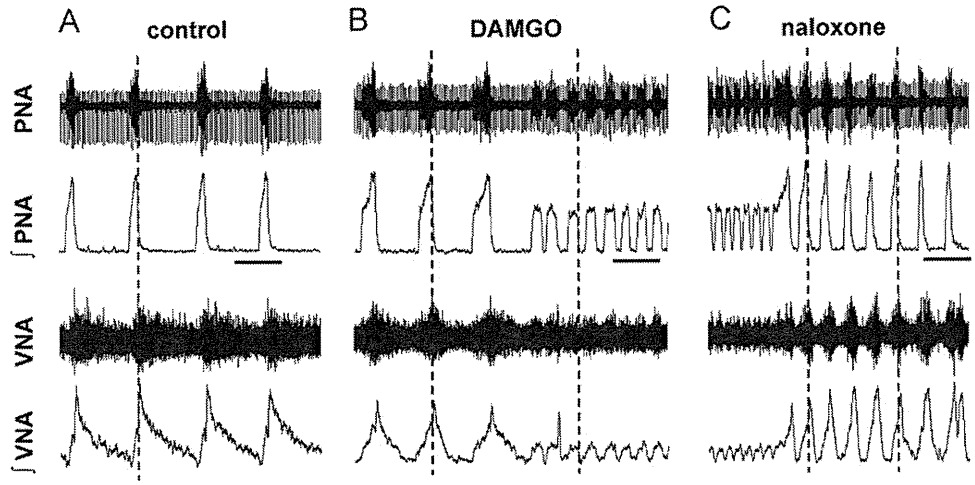

Fig. 2. Comparison of responses of the phrenic and central vagal nerve activities to DAMGO application. On each panel, the top trace is the raw phrenic nerve activity (PNA), the second trace is the integrated phrenic nerve activity (∫PNA), the third trace is the raw central vagal nerve activity (VNA), and the bottom trace is the integrated central vagal nerve activity (∫VNA). Dotted lines indicate offset of inspiration. Bars, 10 s. (A) Nerve activities in the control period. Note that the post-inspiratory component of the central vagal nerve activity is much greater than the inspiratory component. (B) DAMGO application induced the rapid breathing with extremely short T_e. During this breathing pattern, both nerve activities were almost exclusively inspiratory. Note that the inspiratory component of the central vagus nerve was lengthened and the post-inspiratory component already shortened before the rapid breathing pattern emerged. Also note that the transition of breathing pattern occurred within a single breath. (C) Naloxone reversed these changes in breathing pattern. Note that the respiratory cycle time variation was associated with irregular post-inspiratory activity of the central vagus nerve.

2. Materials and methods

Experimental protocols were approved by the Animal Experiment Committee of the University of Tsukuba. Experiments were performed on male Wistar rats (57–100 g, $n = 13$) using the arterially perfused *in situ* preparation (Paton, 1996). Briefly, each animal was deeply anesthetized with isoflurane (Dainippon Sumitomo Pharma, Osaka, Japan), quickly bisected sub-diaphragmatically, and precollicular decerebration was performed. The descending aorta was cannulated with a double lumen catheter (4 F, Braintree Scientific, MA, USA) and retrogradely perfused with a Ringer solution containing an oncotic agent (Ficoll®70, 1.25%, Sigma, MO, USA), gassed with 95% O2 and 5% CO2, warmed to 31 °C, and filtered (polypropylene mesh, 25 μm). Pump flow rate was adjusted to give a perfusion pressure of 60–80 mmHg as monitored via a pressure transducer (MPU-0.5, Nihon Kohden, Tokyo Japan). Neuromuscular paralysis was produced by addition of vecuronium bromide (4 mg/L, Sankyo, Tokyo, Japan) directly to the perfusate. The phrenic and vagus nerves were unilaterally sectioned, and efferent phrenic and vagal nerve discharges were recorded at their central cut ends via glass suction electrodes, amplified, and bandpass filtered (100–3000 Hz) using a bioelectric AC amplifier (AB-610J, Nihon Kohden, Tokyo, Japan). The filtered signals were half-rectified and integrated using a 'leaky' integrator (Spike2, CED, Cambridge, UK) with a time constant of 100 ms. The raw and integrated signals were stored on a hard disk, and analyses of signals were made using Matlab subsequently (MathWorks, Natick, MA, USA). DAMGO and naloxone hydrochloride were both purchased from Sigma (St. Louis, MO, USA). Data were shown as mean ± standard deviation, and statistically analyzed using a paired *t*-test. A p-value < 0.05 was considered significant.

3. Results

To evaluate the effects of DAMGO on the respiratory activity, we first added DAMGO to the perfusate so that the DAMGO concentration in the perfusate was 200 nM. We subsequently increased the DAMGO concentration by 50–200 nM every 5–10 min to a final concentration of 300–1800 nM for evaluating concentration-dependent changes in breathing. Fig. 1 shows a representative time course of respiratory cycle time (T_{tot}), inspiratory time (T_i), expiratory time (T_e), and the amplitude of integrated phrenic nerve activity. DAMGO application (filled arrowheads in Fig. 1A) gradually increased T_i and decreased T_e (Fig. 1Ab and B) with a delay of 5–10 min from the first DAMGO injection into the perfusate reservoir (large filled arrowhead in Fig. 1A). Subsequently, breathing pattern changed dramatically with remarkable shortening of T_e (control 3.9 ± 1.3 s; DAMGO 0.34 ± 0.14 s, $p < 0.0001$) and T_{tot} (control 5.3 ± 1.4 s; DAMGO 1.8 ± 0.9 s, $p < 0.0001$) and with reduction of the amplitude of integrated phrenic nerve activity (35.3 ± 7.8% of control; Fig. 1Ac and B). The change in T_i did not show a consistent tendency. The transition of breathing pattern was within a single respiratory cycle in 10 of 13 preparations, however, a transitional period in which eupnea and the rapid breathing with extremely short T_e and increased T_i/T_{tot} were interchangeably observed in 3 preparations (Fig. 1C). This rapid breathing pattern was distinct from either the classic rapid shallow breathing with inspiratory-to-expiratory (I–E) ratio of 50:50 (Winning and Widdicombe, 1976) or the classic apneustic breathing with a slow respiratory rate because the I–E ratio was approximately 80:20 and the respiratory rate was much faster. The rapid breathing was typically observed at 300–500 nM DAMGO, and additional DAMGO application up to 1800 nM did not change breathing parameters significantly. Further increase in DAMGO concentration (up to 3400 nM) caused apneusis, slowing of respiratory rhythm, and instability of phrenic motor output, however, the response was not consistent. Apnea was not observed. In all preparations, 10 μM naloxone (applied into the perfusate reservoir at open arrow head in Fig. 1A) reversed changes in breathing pattern, however, the respiratory cycle time showed a large variability (Fig. 1Ad and B). Throughout the experiments, quantal slowing as seen *in vitro* (Mellen et al., 2003) of the respiratory rhythm was not observed.

To test whether the observed changes in breathing pattern are mediated peripherally through vagal afferents, we performed bilateral midcervical vagotomy in 3 preparations. Vagotomy did not induce any change in breathing pattern (Fig. 1D), and DAMGO produced a qualitatively identical response with that observed with vagi intact suggesting that the observed rapid breathing was of central nervous system origin.

To obtain mechanistic insights of breathing pattern changes, we simultaneously recorded phrenic and central vagal nerve activities ($n = 4$). All preparations exhibited qualitatively the same results.

Table 1
Effects of DAMGO on the central vagal nerve activity ($n=4$).

	T_i (s)	T_{pi} (s)	T_{e2} (s)	T_{tot} (s)
Control	1.2 ± 0.3	3.8 ± 1.8	0.8 ± 0.6	5.8 ± 2.0
DAMGO	1.7 ± 0.6	1.8 ± 1.1	1.1 ± 0.7	4.6 ± 1.9

Parameters are 5-min averages during the control period (control) and the period just before the transition to the rapid breathing (DAMGO). T_i, T_{pi}, T_e, T_{tot} denote durations of inspiratory component and post-inspiratory component of the central vagal activity, the duration of the expiratory (E2) phase, and the respiratory cycle time, respectively. Values are presented as mean ± standard deviation. Note that DAMGO shortens the post-inspiratory component.

As represented in Fig. 2, the central vagal nerve activity consisted of inspiratory and post-inspiratory components where the post-inspiratory component dominated, and the activity reached its peak just after the offset of inspiration during the control period (Fig. 2A). These activity characteristics contrasted with those of the phrenic nerve activity where the inspiratory component dominated and the peak reached just before the offset of inspiration. After DAMGO application, the inspiratory component was gradually augmented in both phrenic and central vagal nerve activities (Fig. 2B). The post-inspiratory after-discharge was augmented in 6 of 13 preparations (see Fig. 1Ab for an activated example), however, the post-inspiratory component of the central vagal nerve activity was gradually and consistently shortened. These changes of the central vagal nerve activity are summarized in Table 1. On the phase transition to the rapid breathing pattern, the post-inspiratory phase of the central vagal nerve activity was almost abolished, and both the phrenic and vagal nerve activities exhibited the inspiratory phase-dominant pattern. Naloxone reversed breathing pattern (Fig. 2C), however, the post-inspiratory activity of the central vagus nerve remained irregular for more than 10 min, suggesting that variability in T_e and T_{tot} during this recovery period (Fig. 1B) was caused by the instability of the central respiratory pattern generator at the post-inspiratory phase.

4. -Discussion

4.1. Major findings

Application of DAMGO (300–500 nM) to the perfusate consistently induced rapid breathing. T_e was shortened dramatically. The transition from eupnea to rapid breathing was abrupt, but in 3 of 13 preparations these two patterns were intermingled, suggesting that the respiratory oscillator could become bistable at the transition. Elevation of the DAMGO concentration up to 1800 nM did not affect the rapid breathing pattern. Further higher concentrations of DAMGO (up to 3400 nM) caused apneusis, respiratory slowing and phrenic instability, but not apnea. We suspect that apnea may not be brought about by DAMGO with even higher doses. Czapla et al. (2000) reported that in conscious, freely behaving adult rats, endogenous μ-opioid receptor agonists endomorphin 1 (EM1) and 2 (EM2), and the selective μ-opioid receptor agonist DAMGO elicited biphasic ventilatory responses, with marked, short-lived ventilatory depression followed by more sustained increases in ventilation. They did not describe specific changes in respiratory parameters such as respiratory rate, tidal volume, T_i, and T_e. Therefore, we cannot evaluate the similarity or the dissimilarity between respiratory responses with our intra-arterially perfused *in situ* rats and their conscious, freely behaving rats. However, it is clear that respiratory responses to systematically applied DAMGO are different between neonatal *in vitro* preparations and more intact adult preparations generating a 3-phase rhythm.

DAMGO shortened the duration of the post-inspiratory component of the central vagal nerve activity consistently. The shortening of the post-inspiratory phase mimics the early phase (2–3 min) response to intravenously administered morphine (Haji et al., 2003). The post-inspiratory activity was obliterated during the rapid breathing period, suggesting that the respiratory pattern switched from 3-phase to 2-phase. However, this phase transition is not similar to the phase switching to apneusis described previously (Smith et al., 2007), because the 2-phase pattern in the present study was rapid breathing with an extremely shortened T_e. To the best of our knowledge, a rapid breathing pattern in which post-inspiration is obliterated in the presence of DAMGO has never been reported previously. The application of other μ-opioid agonists, i.e., fentanyl and remifentanyl, to *in situ* preparation (Manzke et al., 2009) slows down the respiratory rhythm without a transient increase in respiratory rate. The apparent discrepancy may be explained at least partly by the differences in pharmacological characteristics of the μ-opioid receptor agonists used (Saidak et al., 2006). For example, DAMGO, morphine, EM1 and EM 2 have different potencies for the two G_α proteins, $G_{\alpha i1}$ and $G_{\alpha oA}$.

4.2. Peripheral vs. central effects

Since μ-opioid receptors are present in vagal afferents (Aicher et al., 2000), the observed rapid breathing could be mediated by peripheral mechanisms involving reflex pathways from rapidly adapting receptors or J receptors. However, bilateral vagotomy at the midcervical level did not alter the response, indicating that this is not the case. In addition, peripheral chemoreceptor activation by cyanide decreased T_{tot} and augmented the amplitude of integrated phrenic nerve activity (data not shown), but did not mimic the DAMGO-induced rapid breathing with remarkably shortened T_e and decreased amplitude of the integrated phrenic nerve activity. Therefore, we suggest that the response originated via a central action of DAMGO. This is consistent with the observation that an intracisternally administered μ-opioid receptor agonist increased the respiratory rate (Schaeffer and Haddad, 1985). However, Matsumura et al. (1992) concluded that DAMGO does not cross the blood–brain barrier. This apparent contradiction could partly be explained as follows. In the arterially perfused *in situ* preparation, the perfusate can easily leak out, since small vessels are cut and left open. Therefore, the brainstem could have an access through the surface to drugs within the perfusate after a certain delay, even if they do not cross the blood brain barrier. This is in agreement with the observed 5–10 min delay of the respiratory response after the application of DAMGO. Further, Czapla et al. (2000) argued that the ventilatory increase elicited by systemic injections of EM1, EM2, and DAMGO originated centrally rather than peripherally, because the response was not abolished by naloxone methiodide, which does not cross the blood–brain barrier. Since opioids were applied intravenously in their experiments, it could be argued that DAMGO does cross the blood–brain barrier in the rat, again consistent with the present data. Lonergan et al. (2003) showed that EM1 microinjected into the Bötzinger complex and preBötC consistently increased respiratory rate in anesthetized adult rats. Therefore, these respiratory regions, depressed by DAMGO in neonatal periods, appear to be stimulated by DAMGO in adult rats. Alternatively, other respiratory neurons in the pons or rostral medulla may be responsible for the observed respiratory responses (Tanabe et al., 2005).

In summary, a μ-opioid receptor agonist DAMGO applied to the perfusate of the arterially perfused *in situ* preparation evoked instantaneous phase transition, i.e., eupnea abruptly changed to the rapid breathing with remarkable reduction of expiratory time. Changes in central vagal nerve activity suggest that DAMGO obliterated the post-inspiratory activity and switched the breathing pattern from 3-phase to 2-phase. Loss of post-inspiration may compromise ventilation and coordination of spinal and cranial motor outflows as well as vital reflex responses such as swallow-

ing. It would not, however, be predicted to compromise upper airway patency given that laryngeal adductors would be quiescent. Our results together with previous reports indicate that effects of μ-opioid agonists on breathing are heterogeneous presumably depending on the agonist used, the root of agonist application, and the age and type of animal preparation. We suggest that a μ-opioid agonist with less respiratory depression, such as DAMGO, might be useful clinically and developed for such use.

Acknowledgments

This study was supported by the Grant-in-Aid for Scientific Research by the Ministry of Education, Science, Sports and Culture of Japan (20500360 and 20590218). JFRP was in receipt of a Royal Society Wolfson Research Merit Award.

References

Aicher, S.A., Goldberg, A., Sharma, S., Pickel, V.M., 2000. μ-Opioid receptors are present in vagal afferents and their dendritic targets in the medial nucleus tractus solitarius. J. Comp. Neurol. 422, 181–190.

Chamberlin, N.L., Mansour, A., Watson, S.J., Saper, C.B., 1999. Localization of mu-opioid receptors on amygdaloid projection neurons in the parabrachial nucleus of the rat. Brain Res. 827, 198–204.

Czapla, M.A., Gozal, D., Alea, O.A., Beckerman, R.C., Zadina, J.E., 2000. Differential cardiorespiratory effects of endomorphin 1, endomorphin 2, DAMGO, and morphine. Am. J. Respir. Crit. Care Med. 162, 994–999.

Haji, A., Okazaki, M., Ohi, Y., Yamazaki, H., Takeda, R., 2003. Biphasic effects of morphine on bulbar respiratory neuronal activities in decerebrate cats. Neuropharmacology 45, 368–379.

Hickey, R.F., Severinghaus, J.W., 1981. Regulation of breathing: drug effects. In: Hornbein, T.F. (Ed.), Regulation of Breathing. Part II., New York. , pp. 1251–1312.

Krause, K.L., Neumueller, S.E., Marshall, B.D., Kiner, T., Bonis, J.M., Pan, L.G., Qian, B., Forster, H.V., 2009. μ-Opioid receptor agonist injections into the presumed pre-Bötzinger complex and the surrounding region of awake goats do not alter eupneic breathing. J. Appl. Physiol. 107, 1591–1599.

Lonergan, T., Goodchild, A.K., Christie, M.J., Pilowsky, P.M., 2003. Mu opioid receptors in rat ventral medulla: effects of endomorphin-1 on phrenic nerve activity. Respir. Physiol. Neurobiol. 138, 165–178.

Manzke, T., Dutschmann, M., Schlaf, G., Morschel, M., Koch, U.R., Ponimaskin, E., Bidon, O., Lalley, P.M., Richter, D.W., 2009. Serotonin targets inhibitory synapses to induce modulation of network functions. Philos. Trans. R. Soc. Lond. B: Biol. Sci. 364, 2589–2602.

Manzke, T., Niebert, M., Koch, U.R., Caley, A., Vogelgesang, S., Hulsmann, S., Ponimaskin, E., Muller, U., Smart, T.G., Harvey, R.J., Richter, D.W., 2010. Serotonin receptor 1A-modulated phosphorylation of glycine receptor a3 controls breathing in mice. J. Clin. Invest. 120, 4118–4128.

Matsumura, K., Abe, I., Tominaga, M., Tsuchihashi, T., Kobayashi, K., Fujishima, M., 1992. Differential modulation by μ- and δ-opioids on baroreceptor reflex in conscious rabbits. Hypertension 19, 648–652.

Mellen, N.M., Janczewski, W.A., Bocchiaro, C.M., Feldman, J.L., 2003. Opioid-induced quantal slowing reveals dual networks for respiratory rhythm generation. Neuron 37, 821–826.

Paton, J.F.R., 1996. A working heart-brainstem preparation of the mouse. J. Neurosci. Methods 65, 63–68.

Saidak, Z., Blake-Palmer, K., Hay, D.L., Northup, J.K., Glass, M., 2006. Differential activation of G-proteins by mu-opioid receptor agonists. Br. J. Pharmacol. 147, 671–680.

Schaeffer, J.I., Haddad, G.G., 1985. Regulation of ventilation and oxygen consumption by δ- and μ-opioid receptor agonists. J. Appl. Physiol. 59, 959–968.

Smith, J.C., Abdala, A.P., Koizumi, H., Rybak, I.A., Paton, J.F., 2007. Spatial and functional architecture of the mammalian brain stem respiratory network: a hierarchy of three oscillatory mechanisms. J. Neurophysiol. 98, 3370–3387.

Stucke, A.G., Zuperku, E.J., Sanchez, A., Tonkovic-Capin, M., Tonkovic-Capin, V., Mustapic, S., Stuth, E.A., 2008. Opioid receptors on bulbospinal respiratory neurons are not activated during neuronal depression by clinically relevant opioid concentrations. J. Neurophysiol. 100, 2878–2888.

Tanabe, A., Fujii, T., Onimaru, H., 2005. Facilitation of respiratory rhythm by a mu-opioid agonist in newborn rat pons-medulla-spinal cord preparations. Neurosci. Lett. 375, 19–22.

Winning, A.J., Widdicombe, J.G., 1976. The effect of lung reflexes on the pattern of breathing in cats. Respir. Physiol. 27, 253–266.

PAIN® 152 (2011) 2085–2097

PAIN®

www.elsevier.com/locate/pain

Spatiotemporal and anatomical analyses of P2X receptor-mediated neuronal and glial processing of sensory signals in the rat dorsal horn

Ryoma Aoyama [a], Yasumasa Okada [b,*], Shigefumi Yokota [c], Yutaka Yasui [d], Kentaro Fukuda [a], Yoshio Shinozaki [a], Hideaki Yoshida [a], Masaya Nakamura [a], Kazuhiro Chiba [a], Yukihiko Yasui [c], Fusao Kato [d], Yoshiaki Toyama [a]

[a] Department of Orthopaedic Surgery, School of Medicine, Keio University, 35 Shinanomachi, Shinjuku-ku, Tokyo 160-8582, Japan
[b] Department of Medicine, Keio University Tsukigase Rehabilitation Center, 380-2 Tsukigase, Izu City, Shizuoka 410-3215, Japan
[c] Department of Anatomy and Morphological Neuroscience, Shimane University School of Medicine, 89-1 Enya-cho, Izumo 693-8501, Japan
[d] Department of Neuroscience, School of Medicine, Jikei University School of Medicine, 3-25-8 Nishi-Shimbashi, Minato-ku, Tokyo 105-8461, Japan

Sponsorships or competing interests that may be relevant to content are disclosed at the end of this article.

ARTICLE INFO

Article history:
Received 27 February 2011
Received in revised form 27 April 2011
Accepted 12 May 2011

Keywords:
Spinal cord
Voltage imaging
Whole cell patch recording
Immunohistochemistry
Astrocyte
Nociception

ABSTRACT

Extracellularly released adenosine triphosphate (ATP) modulates sensory signaling in the spinal cord. We analyzed the spatiotemporal profiles of P2X receptor-mediated neuronal and glial processing of sensory signals and the distribution of P2X receptor subunits in the rat dorsal horn. Voltage imaging of spinal cord slices revealed that extracellularly applied ATP (5–500 μM), which was degraded to adenosine and acting on P1 receptors, inhibited depolarizing signals and that it also enhanced long-lasting slow depolarization, which was potentiated after ATP was washed out. This post-ATP rebound potentiation was mediated by P2X receptors and was more prominent in the deep than in the superficial layer. Patch clamp recording of neurons in the superficial layer revealed long-lasting enhancement of depolarization by ATP through P2X receptors during the slow repolarization phase at a single neuron level. This depolarization pattern was different from that in voltage imaging, which reflects both neuronal and glial activities. By immunohistochemistry, $P2X_1$ and $P2X_3$ subunits were detected in neuropils in the superficial layer. The $P2X_5$ subunit was found in neuronal somata. The $P2X_6$ subunit was widely expressed in neuropils in the whole gray matter except for the dorsal superficial layer. Astrocytes expressed the $P2X_7$ subunit. These findings indicate that extracellular ATP is degraded into adenosine and prevents overexcitation of the sensory system, and that ATP acts on pre- and partly on postsynaptic neuronal P2X receptors and enhances synaptic transmission, predominantly in the deep layer. Astrocytes are involved in sensitization of sensory network activity more importantly in the superficial than in the deep layer.

1. Introduction

Extracellular adenosine triphosphate (ATP) plays an important role in sensory information processing in the peripheral and central nervous system through ionotropic P2X as well as metabotropic P2Y receptors [8,9,11]. In the spinal cord, primary processing of sensory information conveyed through the dorsal roots is conducted in the dorsal horn, where the superficial and deep layers have distinct function and structure [15]. Peripherally, ATP activates nociceptive terminals and elicits mechanical allodynia by inducing slow desensitizing currents in dorsal root ganglion neurons [67]. In the dorsal horn, ATP, together with transmitted glutamate and other mediators, modulates neuronal activity through the following mechanisms: ATP enhances synaptic transmission by acting on presynaptic P2X receptors [26,45,53]; ATP increases activity of dorsal horn neurons by directly acting on the postsynaptic P2X receptors [4,23,34,63]; ATP augments glycinergic or GABAergic inhibitory neurotransmission [29,35,59,64], and also inhibits dorsal horn neurons after it is hydrolyzed to adenosine and acting at adenosine P1 receptors [60]. Recently it has been recognized that ATP also acts on glial cells and augments or inhibits neuronal network activity though neuron–glia interaction widely in the central nervous system [5,17,19,33,69]. Indeed, contribution of glial cells (especially microglia) to P2X receptor-mediated long-term potentiation has been recently demonstrated in the dorsal horn [24,31,68]. However, the interacting mechanisms through P2X receptor-mediated signaling between neurons and glial cells (especially astrocytes), and the functional and anatomical differences between the superficial and

* Corresponding author. Tel.: +81 558 85 1701; fax: +81 558 85 1810.
E-mail address: yasumasaokada@1979.jukuin.keio.ac.jp (Y. Okada).

0304-3959/$36.00
doi:10.1016/j.pain.2011.05.014

deep layers in P2X receptor-mediated neuron–glia interaction in the sensory information processing in the dorsal horn, have not been fully elucidated. Further, although it is essential in understanding these issues, the expression and distribution of P2X receptor subtypes/subunits in neurons and glial cells in the spinal cord have never been systematically analyzed.

To understand the spatially heterogeneous complex bidirectional interaction between neurons and glial cells through P2X receptors in the dorsal horn, we conducted functional and anatomical analyses of P2X receptor-mediated neuron–glia interaction in sensory signal processing in the dorsal horn. For this purpose we applied an optical recording technique using a voltage-sensitive dye (ie, voltage imaging technique) that is suitable for the analysis of spatiotemporal neural dynamics [56,57]. In addition to the spatiotemporal information as to network behavior, we observed accurate behaviors of single neurons by precisely recording membrane potentials by whole-cell patch clamp method. Further, we systematically conducted immunohistochemical analyses of all 7 P2X receptor subunits in the spinal cord to establish the anatomical basis of P2X receptor-mediated signaling. In the present study, we focused on astrocytes among various types of glial cells, because the role of astrocytes in the neuron–glia interaction in nociception remains poorly understood, although that of microglia has been relatively well elucidated [12,24,31,68]. Preliminary data were reported in a previous abstract [2].

2. Materials and methods

The present study adhered to the guidelines of the Committee for Research and Ethical Issues of the International Association for the Study of Pain, and was approved by the Animal Experiment Committee of Keio University.

2.1. Spinal cord slice preparation

The procedure of making slice preparations was as previously described [22,75]. Briefly, juvenile rats (Wistar, 4–6 days old) of either sex were deeply anesthetized by diethyl ether inhalation, and the cervical spinal cord was quickly isolated. Transverse slices of the cervical spinal cord (C4, C5, or C6 level; single segment thickness; n = 59) with the dorsal roots attached were prepared in an oxygenated mock cerebrospinal fluid (CSF) either with a brain slicer (Microslicer DTK-1000; Dosaka EM, Kyoto, Japan) or manually using fine ophthalmologic scissors, after we confirmed that the manual technique yielded slices that were equivalent to those made with a brain slicer for voltage imaging. Slices for patch clamp experiments were prepared only with a brain slicer.

Slices for optical recording were stained with voltage-sensitive dye (di-4-ANEPPS; Invitrogen, Carlsbad, CA, USA); preparations were immersed in a dye-containing (0.1–0.2 mg/mL) mock CSF that was bubbled with a gas mixture (95% O_2 and 5% CO_2) for 30 minutes at room temperature [22,56,57].

Slice preparations were placed horizontally in a recording chamber (volume 2 mL), and were maintained under superfusion with a mock CSF that was equilibrated with a gas mixture of 95% O_2 and 5% CO_2 (mock CSF pH 7.4) at a rate of 4 mL/min. The composition of a mock CSF was (in mM) 126 NaCl, 5 KCl, 26 $NaHCO_3$, 1.25 NaH_2PO_4, 2 $MgSO_4$, 2 $CaCl_2$, and 11 glucose.

2.2. Induction of neural activity in dorsal horn

Neural activity in the dorsal horn was induced by electrical stimulation of the dorsal roots. A depolarizing square wave electrical current (amplitude 1.5 mA, duration 50 μs) was applied through a glass suction electrode to unilateral dorsal roots with an electrical stimulator (SEN-7103; Nihon Kohden, Tokyo, Japan) [22,75]. Electrical stimulation of the dorsal roots in our experiments is considered to activate both A and C fibers [22].

2.3. Optical recording

Depolarizing activity in the dorsal horn induced by electrical stimulation was analyzed using an optical recording system, MiCAM01 (BrainVision, Tokyo, Japan) [22,75]. Briefly, the recording chamber was placed under an epifluorescent microscope (Eclipse E600FN; Nikon, Tokyo, Japan) with a 4× objective lens (Plan Apo, NA = 0.2, Nikon). Preparations were illuminated through a tungsten-halogen lamp (250 W; Oriel, Stratford, CT, USA), which was driven by a stable DC power source (PD36-20; Kenwood, Tokyo, Japan) through an excitation filter (λ = 535 ± 10 nm). Epifluorescence was detected through a barrier filter (long pass λ > 610 nm) using a MiCAM01-CCD camera (spatial resolution 60 × 90 pixels). The change in fluorescence intensity (ΔF) relative to the initial intensity of fluorescence (F) in each pixel was recorded at a rate of one frame/2 ms (the total recording corresponded to 681 frames). The recording was repeated 10 times at 10-second intervals, and the signals were averaged. The ratio ΔF/F in each pixel was used to normalize unevenness of dye-staining and illumination within the recorded area. Optical signals at 2 representative points (one in the superficial layer and the other in the deep layer) were subjected for analyses. These 2 points were determined as follows: When we observed the inner structure of the transversely cut surface of the spinal cord under a low magnification (4×) microscope, we could delineate the gray matter. The most dorsal part of the gray matter (within 10% of the dorsal side along the dorsoventral axis of the gray matter) was assumed to be the superficial layer, and the neck portion of the dorsal horn (from the dorsal side between 17% and 40% along the dorsoventral axis) was assumed to be the deep layer, referring to the atlas of the spinal cord anatomy [58] and our neuron-specific nuclei N (NeuN) immunohistological pictures (also see Section 2.5. *Immunohistochemistry* for details) [21]. These 2 points approximately corresponded to lamina II and laminae IV-V, respectively, in the post hoc evaluation with histological images.

After the preparations were superfused with a control mock CSF at least 20 minutes to stabilize the slice condition, optical recording was conducted to obtain control data. Then preparations were superfused for 20 minutes with mock CSFs that contained drugs, followed by washout superfusion with a control mock CSF up to 30 minutes.

We tested the effects of (1) ATP (5, 50, and 500 μM) (n = 6, 17, and 7, respectively); (2) ATP (50 μM) in the presence of nonspecific adenosine P1 receptor antagonist theophylline (300 μM) (n = 6) [38]; (3) ectonucleotidase-resistant P2X receptor agonist αβmeATP (50 μM) (n = 5) [37,43,62]; (4) ATP (50 μM) in the presence of purinergic receptor antagonist pyridoxal phosphate-6-azophenyl-2′,4′-disulfonic acid (PPADS) (50 μM) (n = 7) [25,37,43,62]; and (5) ATP (50 μM) in the presence of astrocyte metabolism blocker fluoroacetate (5 mM) (n = 6) [20,30].

All voltage-imaging experiments were conducted at 27–28 °C except for the studies to analyze the influence of low temperature, in which we compared the effects of ATP at a representative concentration (50 μM) at 27–28 °C as the high temperature group (n = 17) and at 23–24 °C as the low temperature group (n = 5). Therefore, the temperature at which experiments were conducted was 27–28 °C unless indicated.

2.4. Whole cell patch recording

The spinal cord slices were made with the same procedures and submerged in and perfused with the same mock CSF as used for

voltage imaging experiments at a rate of 3 mL/min. The recording chamber, in which the slices were secured with nylon mesh attached to a platinum frame, was placed under an upright microscope (BX-50WI; Olympus, Tokyo, Japan) with infrared differential interference contrast optics, and neurons in the dorsal horn were visually identified [32,37,62]. The infrared differential interference contrast images were captured using a chilled CCD camera (C5985-02; Hamamatsu Photonics, Hamamatsu, Japan) and stored digitally. Patch clamp electrodes were made from borosilicate glass pipettes (1B120F-4; World Precision Instruments, Sarasota, FL, USA). The composition of the intrapipette solution was (in mM) 120 gluconic acid potassium, 6 NaCl, 1 $CaCl_2$, 2 $MgCl_2$, 2 ATP Mg, 0.5 GTP Na, 5 EGTA, 10 HEPES hemisodium, 12 Na_2 phosphocreatine (pH 7.2 adjusted with KOH; osmolarity 310 mOsm/kg). The tip resistance of the electrode was 3–6 MΩ. The membrane potential was recorded from neurons in the superficial layer (the inner layer of lamina II) under whole-cell configuration. Six neurons recorded in 6 spinal cord slices from 3 rats were used for whole-cell recordings. The dorsal roots were stimulated using the same types of suction electrodes with the same intensity and duration as those used in the voltage imaging described above. Membrane potential changes induced by dorsal root stimulation were recorded with a patch clamp amplifier (Axopatch 200B; Axon Instruments, Foster City, CA, USA) with a current clamp mode and sampled at 16-bit resolution at 10 kHz (LabChart; ADInstruments, Colorado Springs, CO, USA). Effects of extracellularly applied ATP on membrane potentials were examined by bath-applying ATP (50 μM). All recordings were made in the presence of 8-cyclopentyl-1,3-dipropylxanthine to block P1 receptors at 27–28 °C. The averaged evoked potentials and their time course were analyzed with IgorPro (ver.5; WaveMetrics, Portland, OR, USA).

2.5. Immunohistochemistry

The distributions of cell markers for neurons (NeuN) and astrocytes (GFAP and S-100β) and those of all 7 types of P2X ($P2X_1$–$P2X_7$) receptor subunits in the cervical spinal cord were analyzed by immunohistochemistry. We adopted 2 important astrocyte markers, GFAP and S-100β, that could be differently expressed during the perinatal developmental period, for our extensive analysis of astrocyte organization in the spinal cord [7]. The technique of immunostaining was as previously described [74]. Briefly, juvenile rats (Wistar, 4–6 days old, n = 12) were deeply anesthetized and perfused transcardially with 10 mL of saline, followed by 20 mL of 4% paraformaldehyde in 0.1 M phosphate buffer (PB, pH 7.3). The spinal cords were removed, postfixed in the same fixative overnight at 4 °C, and then immersed in cold 20% sucrose in PB (pH 7.3). Subsequently, the spinal cords (C4–C6 level) were cut into 40-μm-thick sections on a freezing microtome. The sections were washed in phosphate-buffered saline (PBS, pH 7.3), incubated in blocking solution composed of 3% normal donkey serum and 0.2% Triton-X in PBS for 30 minutes, and then incubated overnight in blocking solution containing mouse anti-NeuN, mouse anti-GFAP, mouse anti-S-100β, or rabbit anit-P2X receptor subunit antibodies (see Table 1 for details of each antibody). Subsequently, the sections were washed in PBS, incubated in blocking solution containing biotinylated donkey anti-mouse immunoglobulin G (IgG; Jackson ImmunoResearch Laboratories, West Grove, PA, USA; 1:500) for NeuN, GFAP, and S-100β or biotinylated donkey anti-rabbit IgG for P2X receptor subunits (Jackson ImmunoResearch Laboratories; 1:500) for 4 hours, washed again in PBS, and then incubated in PBS containing avidin–biotin–peroxidase complex (Vector Laboratories, Burlingame, CA, USA; 1:100) for 1 hour. After being washed in PBS, the sections were incubated in 25 mL of 0.1 M PB containing 10 mg diaminobenzidine and 10 μL of 30% hydrogen peroxide. Subsequently, the sections were mounted onto gelatinized slides, coverslipped with Canada balsam (Wako Pure Chemical Industries, Osaka, Japan), and observed under a light microscope (Eclipse E800; Nikon). In the absence of primary antibody, no positive immunoreactivity was observed. Specificity of antibodies for $P2X_{1-4}$ and $P2X_7$ subunits was confirmed by absorption controls. These antibodies were preabsorbed with excess amount of appropriate immunogen (25 μg/mL) and then applied to tissue sections. Preabsorption reduced the staining to background levels.

Table 1
Primary antibody information.

Antigen	Source, Cat. No.	Working dilution
$P2X_1$	Alomone Labs (Jerusalem, Israel), APR-001	1:1000; LM, 1:500; FM
$P2X_2$	Alomone Labs (Jerusalem, Israel), APR-003	1:1000; LM
$P2X_3$	Alomone Labs (Jerusalem, Israel), APR-016	1:1000; LM, 1:1000; FM
$P2X_4$	Alomone Labs (Jerusalem, Israel), APR-002	1:1000; LM, 1:500; FM
$P2X_5$	Lifespan Bioscience (Seattle, WA, USA), NBP1-20178	1:1000; LM, 1:500; FM
$P2X_6$	Novus Biologicals (Littleton, CO, USA), LS-B 154	1:4000; LM, 1:1000; FM
$P2X_7$	Alomone Labs (Jerusalem, Israel), APR-004	1:1000; LM, 1:500; FM
NeuN	Chemicon/Millipore (Billerica, MA, USA), MAB377	1:200; LM, 1:200; FM
GFAP	Millipore (Billerica, MA, USA), MAB360	1:5000; LM, 1:2000; FM
S-100β	Sigma-Aldrich (St. Louis, MO, USA), S2532	1:5000; LM, 1:2500; FM

LM, light microscopy; FM, fluorescent microscopy; NeuN, neuron-specific nuclei N; GFAP, glial fibrillary acidic protein; S-100β, S-100-protein β-subunit.

For double immunofluorescent histochemistry, spinal cord sections (40 μm thick) were prepared as described above. The sections were incubated in blocking solution for 30 minutes and subsequently incubated overnight in blocking solution containing a combination of antibodies of cell markers and P2X receptor subunits. After being washed in PBS, the sections were incubated in blocking solution containing Alexa488-conjugated anti-rabbit IgG (Invitrogen; 1:500) and Cy5-conjugated anti-mouse IgG (Jackson Immunoresearch Laboratories; 1:500) for 3 hours. Subsequently, the sections were mounted onto gelatinized slides coverslipped with vectashield (Vector Laboratories). Finally, the sections were observed under a confocal laser-scanning microscope (FV300; Olympus), and the distribution of P2X receptor subunits in identified neurons and astrocytes were analyzed by double labeling with antibodies against P2X receptor subunits and those against NeuN, GFAP, or S-100β. Cytoarchitecture of the spinal cord was evaluated based on the previous report [50] and the anatomical atlas [58].

2.6. Statistical analysis

Statistical analyses were conducted mostly using 1-way analysis of variance followed by either Tukey–Kramer or Fisher protected least-significant-difference post hoc multiple comparison, as indicated. However, for paired data, paired *t*-test was used. Values are expressed as mean ± SEM. $P < 0.05$ was considered statistically significant.

3. Results

3.1. Voltage imaging

3.1.1. Depolarizing optical signals induced by dorsal roots stimulation

Electrical stimulation of the unilateral dorsal roots evoked depolarizing optical signals ipsilaterally, mainly in laminae I–V in

the dorsal horn. The depolarizing activity started at the dorsal root entry zone and extended to the medial and ventral direction. The depolarization wave reached the lateral half of the superficial layer (lamina II) in 2 ms after stimulation (Fig. 1A, 2 ms), and the depolarized region expanded ventromedially within 6 ms after stimulation (Fig. 1A, 6 ms). Within 10 ms after stimulation, the depolarized region extended medially near to the midline of the superficial layer and to the intermediate (lamina III) and deep (laminae IV–V) layers (Fig. 1A, 10 ms). Then, gradual repolarization occurred, but depolarization lasted predominantly in the superficial layer up to several hundred milliseconds (Fig. 1A, 200 and 400 ms).

The depolarizing optical signals in the superficial and deep regions consisted of 2 components; a fast component, which rose

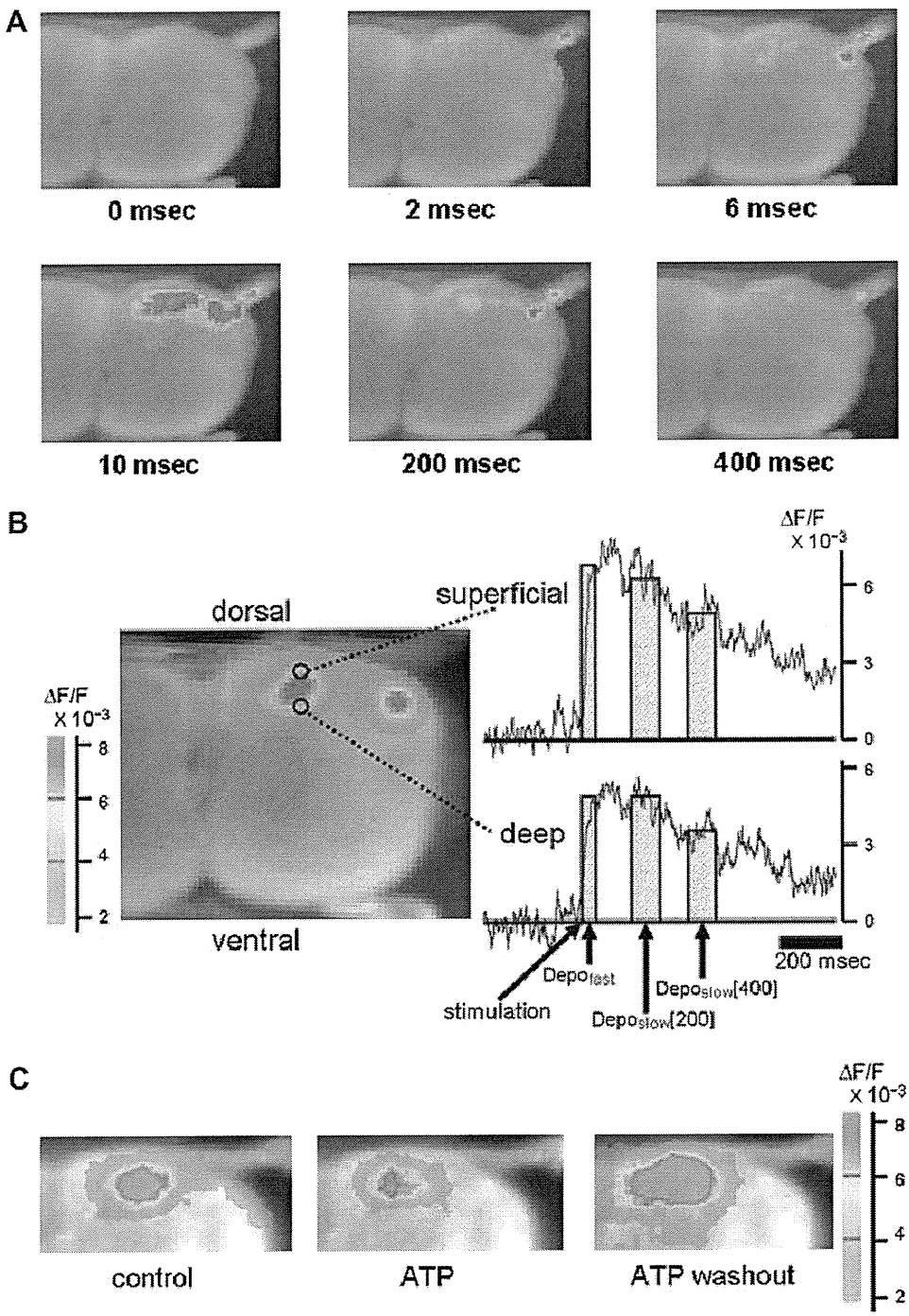

Fig. 1. (A) Examples of time-series voltage imaging data. When the dorsal roots (shown at the right upper corner in each panel) were stimulated, depolarization rapidly extended in the dorsal horn from the superficial layer to the deep layer, followed by gradual repolarization. At 200 and 400 ms after stimulation, depolarization persisted predominantly in the superficial layer. For pseudocolor scaling of the optical signal intensity, see panel B. (B) Examples of voltage imaging and depolarizing optical signal data. Left: A depolarized region in the dorsal horn at 200 ms after stimulation of the dorsal roots is shown by pseudocolor that reflects fluorescence changes (ΔF/F). Right: Temporal sequences of depolarizing optical signals (membrane potential trajectories) at the superficial and deep regions. Amplitudes of fast and slow components were indexed as $depo_{fast}$, $depo_{slow}$[2 0 0], and $depo_{slow}$[4 0 0] that were normalized as% of control. (C) Example of voltage imaging data showing the effects of adenosine triphosphate (ATP) and its washout. During superfusion with a mock cerebrospinal fluid containing ATP (50 μM), the depolarized region became smaller as compared to the control. After ATP was washed out, the post-ATP rebound potentiation was observed, that is, the depolarizing optical signals were augmented and the depolarized region was enlarged, especially toward the deep layer.

rapidly and occasionally formed a peak shape with a short duration (⩽20 ms after stimulation), and a slow component, which followed the fast component and gradually decayed (duration >800 ms) [22,75]. In the subsequent pharmacological analyses, effects of drugs in these 2 points were evaluated as relative changes in depolarizing optical signal amplitudes at 8–20 ms after stimulation for a fast component (a peak value between 0 ms and 20 ms after stimulation was adopted, referred to as $depo_{fast}$) and those at 200 ms and 400 ms after stimulation for slow components (average values between 150 ms and 248 ms and between 350 ms and 448 ms, referred to as $depo_{slow}$[2 0 0] and $depo_{slow}$[4 0 0], respectively) (Fig. 1B).

3.1.2. Effects of ATP

The changes in $depo_{fast}$, $depo_{slow}$[2 0 0], and $depo_{slow}$[4 0 0] were evaluated at the following 3 time points: (1) immediately

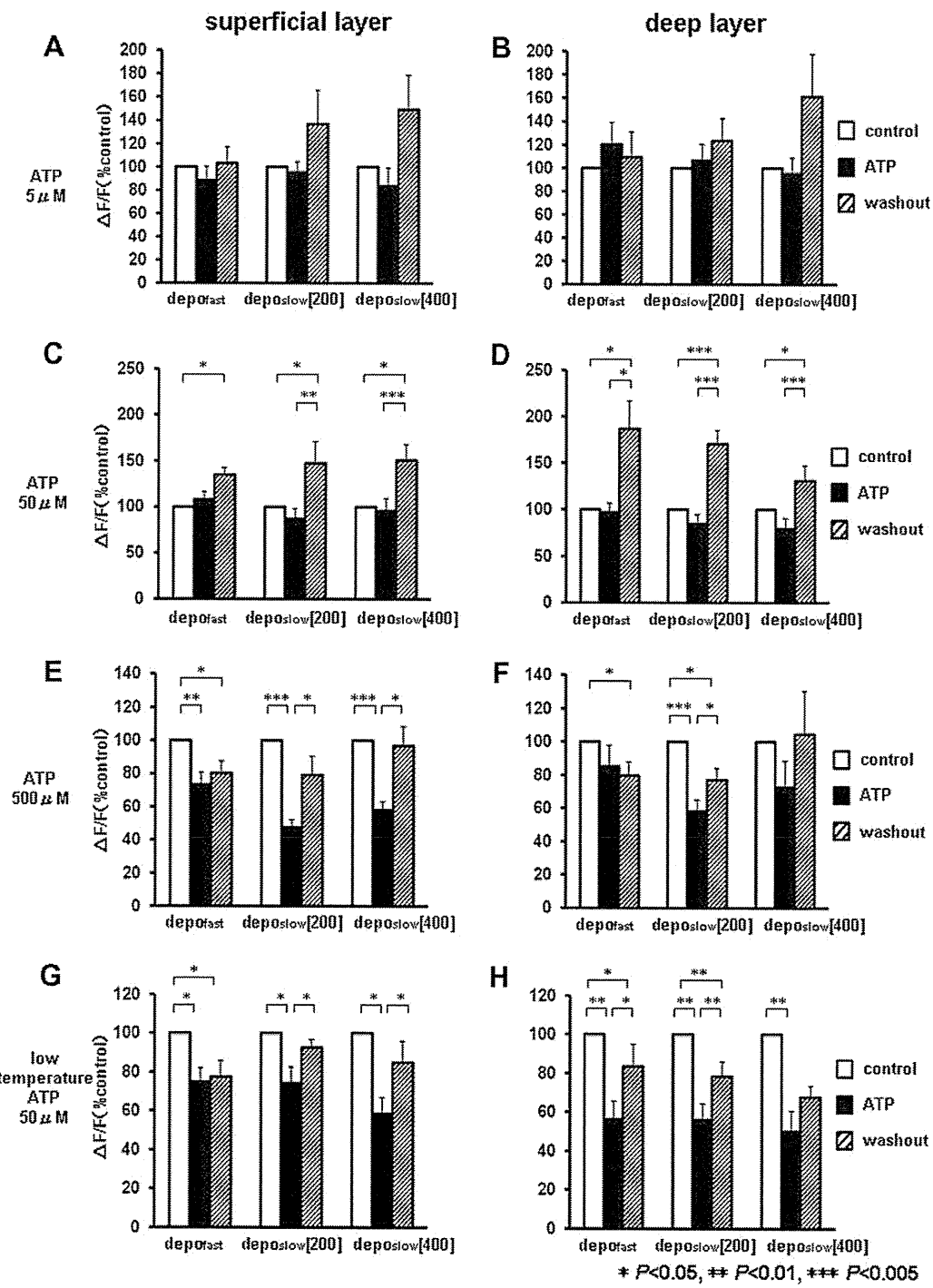

Fig. 2. Effects of extracellularly applied adenosine triphosphate (ATP) on fast and slow components of depolarizing optical signals analyzed by voltage imaging. (A and B) A low concentration (5 μM) of ATP showed no effect. (C and D) A moderate concentration (50 μM) of ATP slightly suppressed the optical signals (statistically not significant) and then clearly induced post-ATP rebound potentiation of optical signals, especially in the deep layer. (E and F) A high concentration (500 μM) of ATP significantly suppressed the amplitudes of depolarizing optical signals while ATP was applied. After ATP was washed out, they were substantially recovered but did not become larger than the control. (G and H) At low temperature, even a moderate concentration of ATP significantly suppressed optical signals, and the post-ATP rebound potentiation was weakened, especially in the deep layer (compare these with high temperature data shown in C and D).

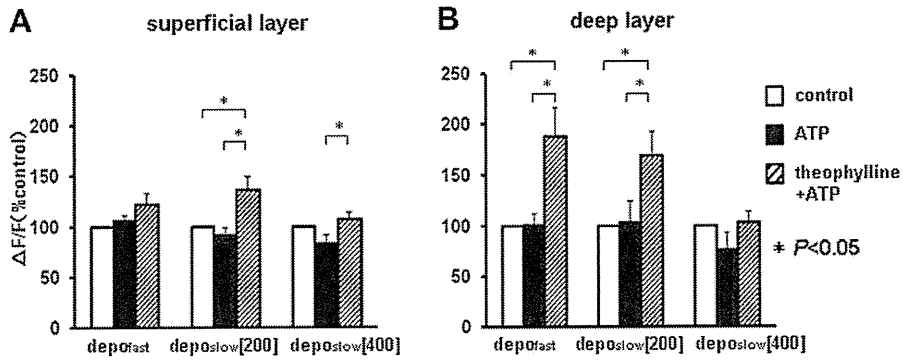

Fig. 3. Effects of adenosine triphosphate (ATP) in the presence of theophylline analyzed by voltage imaging. When pretreated with theophylline, ATP did not suppress but augmented the depolarizing optical signals, especially in the deep layer.

before the ATP application (control); (2) 10 minutes after application (ATP); and (3) 10 minutes after replacement of ATP-containing solution to control mock CSF that did not contain ATP (washout). A low concentration of ATP (5 μM) showed no effect. A moderate concentration of ATP (50 μM) tended to suppress the slow component (statistically not significant) without affecting the fast one in both superficial and deep layers. Interestingly, this effect was followed, after washout of ATP, by potentiation of both fast and slow components (designated as post-ATP rebound potentiation), which was marked in $depo_{fast}$ and $depo_{slow}$[2 0 0] in the deep layer. This post-ATP rebound potentiation was observed for 40–60 minutes after ATP was washed out. A high concentration of ATP (500 μM) significantly suppressed the fast and slow components in both superficial and deep layers. The post-ATP rebound potentiation was manifest only at a moderate concentration (50 μM) (Figs. 1C and 2).

We compared the effects of ATP (50 μM) at high and low temperatures. Attenuation of depolarizing optical signals by ATP was more remarkable at low temperature (23–24 °C) than at high temperature (27–28 °C), and the recovery of depolarizing signals after washout of ATP was weaker at low temperature than at high temperature. This ATP-induced suppression of depolarizing signals at low temperature was observed in both fast and slow components, and was more prominent in the deep layer than in the superficial layer (in Fig. 2, compare C and G for signals in the superficial layer, and D and H for signals in the deep layer).

3.1.3. Effects of ATP in the presence of theophylline

After the effect of ATP (50 μM), including post-ATP rebound potentiation, was recorded as control and after these effects disappeared completely, the effect of ATP (50 μM) was examined in the presence of theophylline (300 μM). Theophylline antagonized ATP-induced suppressive action on depolarization but rather increased signal amplitudes. These effects by theophylline were remarkable in $depo_{fast}$, and in $depo_{slow}$[2 0 0] in the deep layer (Fig. 3).

3.1.4. Effects of αβmeATP

Application of a stable P2X receptor agonist αβmeATP (50 μM) augmented depolarizing signals in both superficial and deep layers, indicating that this signal augmentation is mediated by P2X receptors. In the superficial layer, αβmeATP induced significant augmentation only in slow components, but in the deep layer, αβmeATP enhanced depolarization in both fast and slow components. The depolarization persisted and even further potentiated after washout of αβmeATP, and this persisted depolarization after washout of αβmeATP was prominent in the deep layer (Fig. 4).

3.1.5. Effects of ATP in the presence of PPADS

Attenuation of depolarizing signals induced by ATP (50 μM) was enhanced in both superficial and deep layers in the presence of a P2X receptor antagonist PPADS (50 μM). Also, post-ATP rebound potentiation was not observed either in the superficial or deep layer in the presence of PPADS. This suppressive action of ATP in the presence of PPADS was remarkable in slow components (Fig. 5). These results indicate that augmenting action of ATP through P2X receptors was blocked with PPADS, and as a consequence, ATP-induced suppressive action, which is not P2X receptor-mediated, became more prominent.

3.1.6. Effects of ATP in the presence of fluoroacetate

Suppression of both fast and slow components by ATP (50 μM) was observed by 20-minute pretreatment with fluoroacetate (5 mM) prominently in a superficial layer. Interestingly, the post-

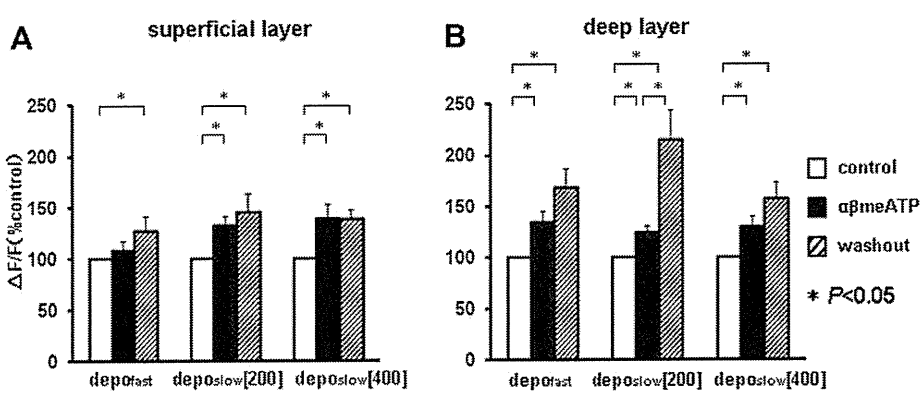

Fig. 4. Effects of αβmeATP analyzed by voltage imaging. Opposite from adenosine triphosphate (ATP), application of αβmeATP did not suppress the depolarizing optical signals but potentiated them. The potentiation persisted and even augmented after αβmeATP was washed out, especially in the deep layer.

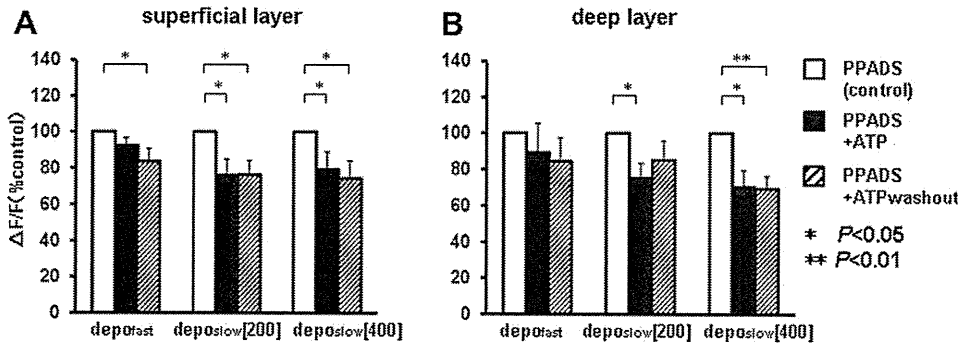

Fig. 5. Effects of adenosine triphosphate (ATP) in the presence of pyridoxal phosphate-6-azophenyl-2′,4′-disulfonic acid (PPADS) analyzed by voltage imaging. When pretreated with PPADS, ATP-induced suppression of the depolarizing optical signals persisted and the post-ATP rebound potentiation was abolished.

ATP rebound potentiation was completely abolished in the presence of fluoroacetate in both superficial and deep layers. Slow components remained suppressed even after washout of ATP in the superficial layer (Fig. 6).

3.2. Effects of ATP on neuronal membrane potential

To complement the drawbacks of the voltage imaging experiments, we made direct recordings of the membrane potential from single neurons in the superficial layer of the dorsal horn, that is, we recorded activities of single neurons while avoiding spatially overlapped signals from multiple neurons and those of glial cells in the regions of interest (Fig. 7A and B). The membrane potential trajectories evoked by the dorsal root stimulation was characterized with a strong and rapid depolarization followed by a repolarization phase with rapid and slow exponential decay components (Fig. 7C). Application of ATP (50 μM) for 10–20 minutes potentiated the depolarization during the repolarization phase appearing 200–400 ms after the dorsal root stimulation (Fig. 7C–E). However, the time course of the recovery during the washout of ATP was thoroughly distinct from and much shorter than that observed by voltage imaging (Fig. 7E and F), suggesting that the persistent membrane potential depolarization after ATP application observed by voltage imaging might contain, in part, the neuronal depolarization, but should largely consist of nonneuronal activities evoked by the dorsal root stimulation.

3.3. Immunohistological analyses

Distributions of immunoreactivity for NeuN, GFAP, and S-100β are shown in Fig. 8. Laminar structure of the gray matter was clearly demonstrated by NeuN immunocytochemistry (Fig. 8A and D). GFAP was strongly positive in white matter, especially in the marginal layer; and GFAP-positive cells with fibrillary processes, apparently fibrous astrocytes, were sparsely scattering in the entire gray matter, and among the dorsal horn layers their distribution was dense in laminae I–II and in the lateral half of laminae V–VI (Fig. 8B and E). S-100β-positive cells were distributed mainly in the gray matter. S-100β immunoreactivity was strongly detected in the marginal layer, and it was predominantly found in laminae I–II and mainly in somata but not in processes in the dorsal horn (Fig. 8C and F).

We analyzed immunohistochemical distributions of all 7 P2X receptor subunits, and found spatially distinct patterns of these distributions. The $P2X_1$ subunit was densely distributed in neuropils in laminae I–II (Fig. 9A and B), apparently as afferent fibers surrounding NeuN-positive cell bodies (Fig. 9C). Specific anatomical relationship between $P2X_1$-positive neuropils and astrocytes was not found (Fig. 9D and E). The $P2X_2$ subunit was weakly positive in fibers in the dorsal roots, and was almost negative in the gray matter (picture not shown). The $P2X_3$ subunit was positive in nerve fibers in the dorsal roots and in neuropils in the dorsal horn (in laminae I–V), with markedly dense distribution in the inner layer of lamina II (Fig. 9F and G), where $P2X_3$-positive neuropils and NeuN-positive cell bodies were intermingled (Fig. 9H). In the dorsal horn $P2X_3$-positive neuropils also appeared to surround astrocytes (Fig. 9I and J). The $P2X_4$ subunit was strongly positive in small cells (possibly in microglia) in the gracile fasciculus and sparsely detected in the entire dorsal horn (Fig. 9K and L). The $P2X_4$ subunit was also positive in nerve fibers entering the dorsal horn and in neuropils that were distributed in the gray matter and around NeuN-positive cell bodies, yet without specific anatomical relationship either with GFAP-positive or with S-100β-positive cells (Fig. 9M–O). Sparse $P2X_5$-positive fibers were distributed in laminae I–III (Fig. 9P and Q), where small-sized NeuN-positive cell bodies but not GFAP- or S-100β-positive cell bodies were also

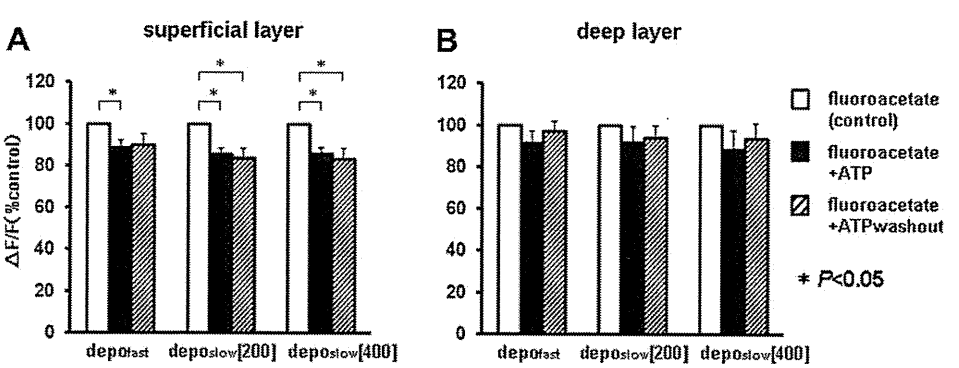

Fig. 6. Effects of adenosine triphosphate (ATP) in the presence of fluoroacetate analyzed by voltage imaging. When pretreated with fluoroacetate, ATP-induced suppression of the depolarizing optical signals persisted even after ATP was washed out and thus the post-ATP rebound potentiation was abolished.

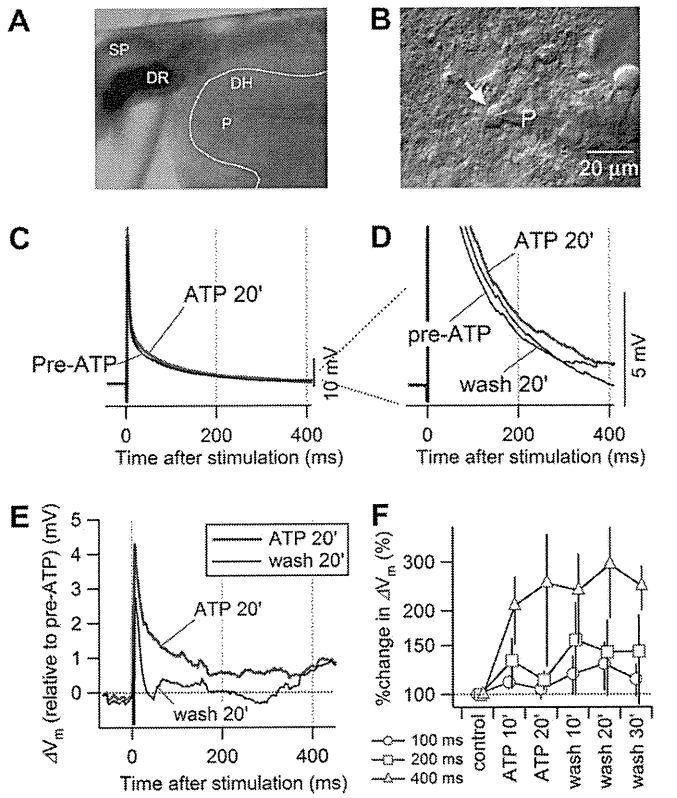

Fig. 7. Effects of adenosine triphosphate (ATP) on dorsal horn-stimulated membrane potential responses in a single neuron analyzed by whole-cell recording. (A and B) Infrared differential interference contrast images of a dorsal horn slice used for whole-cell recordings (A) and an example of a neuron being recorded in the superficial layer (arrow, B). SP, the tip of the suction electrode pipette; DR, dorsal root, DH, dorsal horn; P, recording pipette. (C) Membrane potential responses of a lamina II neuron to the dorsal root stimulation before (black trace, Pre-ATP) and during (red trace, ATP 20′) the application of 50 μM ATP. Averaged waveforms of 10 consecutive trials. (D) The same plot as in C but with larger magnification of the ordinate. Note that 20-minute perfusion of ATP resulted in larger poststimulus depolarization, which recovered almost to the pre-ATP value after 20-minute washout. (E) Traces showing the subtraction of pre-ATP trace from that recorded at 20-minute perfusion of ATP (red trace) and 20-minute washout (black trace). (F) Averaged data of membrane potential amplitude changes at 100 (open circles), 200 (squares), and 400 ms (triangles) after stimulation. Data were normalized as% of control. Depolarization potentiated by ATP during the repolarization phase tended to persist even after ATP was washed out.

immunopositive for $P2X_5$ (Fig. 9R-T). The $P2X_6$ subunit was diffusely distributed in neuropils in the entire gray matter (Fig. 9U and V), but was rather sparse in laminae I–II. $P2X_6$-positive neuropils were intermingled with NeuN-positive, GFAP-positive, and S-100β-positive cell bodies in the dorsal horn (Fig. 9W–Y). The $P2X_7$ subunit was strongly positive in nerve fibers of both dorsal and ventral roots and in S-100β-positive ependymal cells that surrounded the central canal (Fig. 10A). Also, it was positive in neuropils in the entire dorsal horn (Fig. 10B). Although it was found that only NeuN-positive cells were surrounded by $P2X_7$-immunoreactivity (Fig. 10C–E), many GFAP-positive and S-100β-positive cells showed immunoresponses for the $P2X_7$ antibody, especially on and around their cell bodies (possibly in astrocytic processes) in the dorsal horn (Fig. 10F–H and I–K). These results were summarized in Table 2 for comprehension.

4. Discussion

4.1. Validity of the use of the juvenile rat spinal cord

There may be a concern about the validity of the use of the juvenile rat spinal cord and a suspicion as to whether these immature animals show any nociceptive reflex and long-term potentiation in response to noxious stimuli. However, such concerns are unfounded. When we made slice preparations, we carefully monitored the level of anesthesia by pinching the tail as well as the forepaw, neck, and shoulder, which are innervated by the C4–C6 spinal cord. We indeed observed behavioral reflexes in response to pinching of these regions when the anesthetic level was light in these immature animals. Also, it has been reported that rats start showing nociceptive reflexes, and dorsal horn neurons of the cervical spinal cord respond to nociceptive stimuli before birth (by fetal 21st day) [73]. Furthermore, it has been reported that the neuronal circuitry of the rat spinal cord exhibits long-term potentiation in response to peripheral cutaneous nerve stimulation at the latest at 3–7 days after birth [48]. Therefore, the use of the juvenile rat spinal cord in the study of sensory signal processing and its plasticity is validated.

4.2. Effects of extracellularly applied ATP

4.2.1. Suppressive action of ATP on depolarizing optical signals

The observation that the suppressive action of extracellularly applied ATP on depolarizing optical signals reversed into

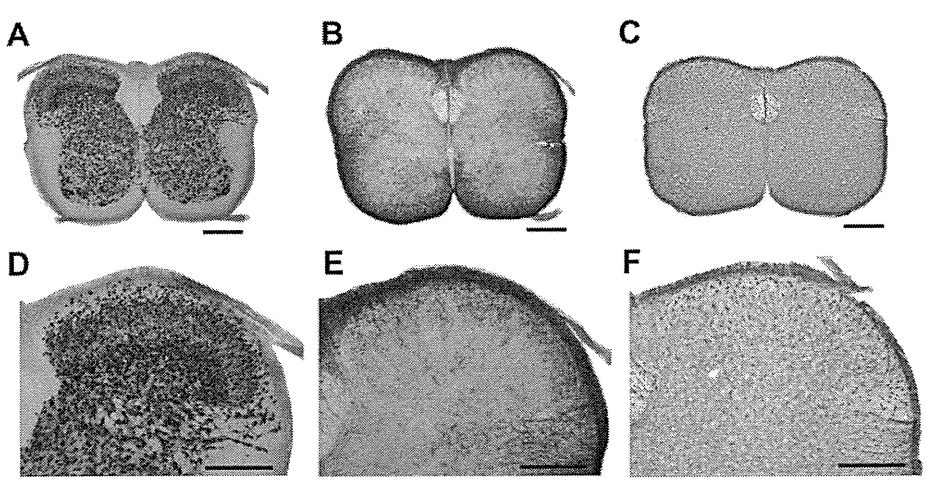

Fig. 8. Distributions of immunoreactivity for neuron-specific nuclei N, (panels A and D), glial fibrillary acidic protein (panels B and E), and S-100-protein β-subunit (panels C and F) in the spinal cord. Panels D–F are enlarged images of the dorsal horn region in panels A, B, and D, respectively. For details see the text. Bar in panels A–C: 300 μm. Bar in panels D–F: 200 μm.

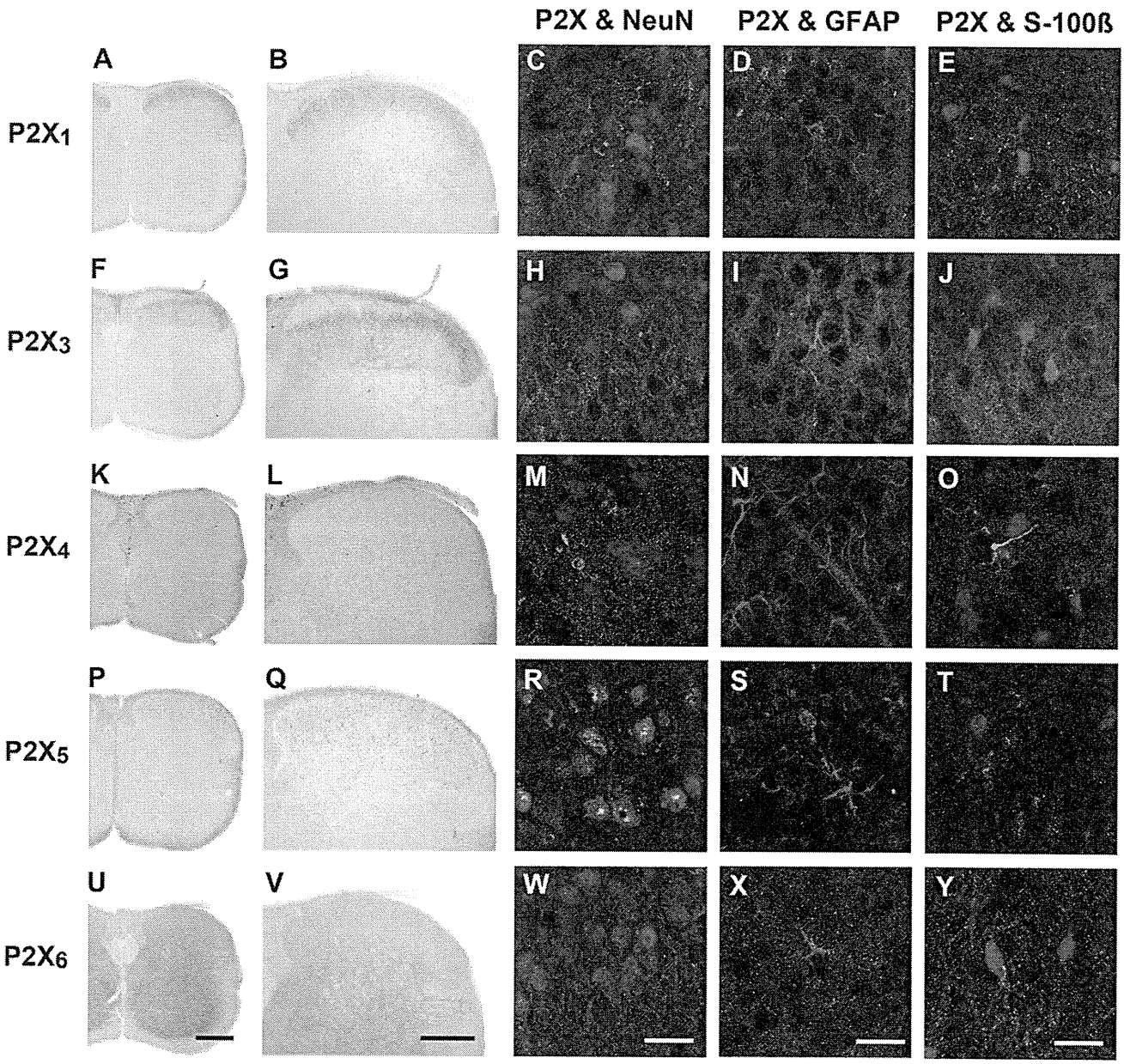

Fig. 9. Distributions of immunoreactivity for P2X receptor subunits in the spinal cord. Immunoreactivity for $P2X_1$ and $P2X_3$-$P2X_6$ is shown in the first column and enlarged in the second column. Double immunofluorescent histochemistry pictures of P2X receptor subunits and either neuron-specific nuclei N (NeuN), glial fibrillary acidic protein (GFAP), or S-100-protein β-subunit (S-100β) with high magnification are shown in the third, fourth, and fifth columns, respectively. Immunoreactivity for P2X receptor subunits is shown as green, and that for NeuN, GFAP, and S-100β is shown as red. For details, see the text. Bar in panel U: 300 μm. Bar in panel V: 200 μm. Bar in panels W, X, and Y: 20 μm.

augmenting one by pretreatment with a nonspecific P1 receptor blocker, theophylline, indicates that adenosine, a degraded product from ATP, suppressed depolarizing optical signals and counteracted the augmenting action of ATP on depolarizing optical signals [52], although ATP-induced augmentation of GABAergic and glycinergic inhibitory neurotransmission might be partially involved [29,59]. Prominent suppression of depolarizing optical signals by a higher concentration of ATP may play a role in preventing overexcitation of the local nociceptive circuitry.

4.2.2. Augmenting action of ATP on depolarizing optical signals

We confirmed by patch clamp recording that the enhancement of depolarizing slow component signals by extracellularly applied ATP is at least partly due to enhanced depolarization of neurons. However, the much slower time course of the depolarizing slow component signals recorded by voltage imaging indicates that those signals reflect depolarization of glial cells (compare Figs. 1A and 7C) [32,39,40,42,49,65]. Further, our observation that astrocyte metabolism blocker fluoroacetate largely diminished the post-ATP rebound potentiation indicates that astrocyte activation accompanied by neuronal activity elicits the depolarizing slow component signals in voltage imaging and it plays a role either directly or indirectly in P2X receptor-mediated long-term potentiation. Although these findings were obtained in acute in vitro experiments, observed P2X receptor-mediated long-term potentiation in our study is compatible with previously reported early-phase phenomenon of the long-lasting allodynia induced in vivo [51,67]. The mechanism of such depolarization potentiation by ATP could be explained as follows: Presynaptic neurons that are once activated by ATP through

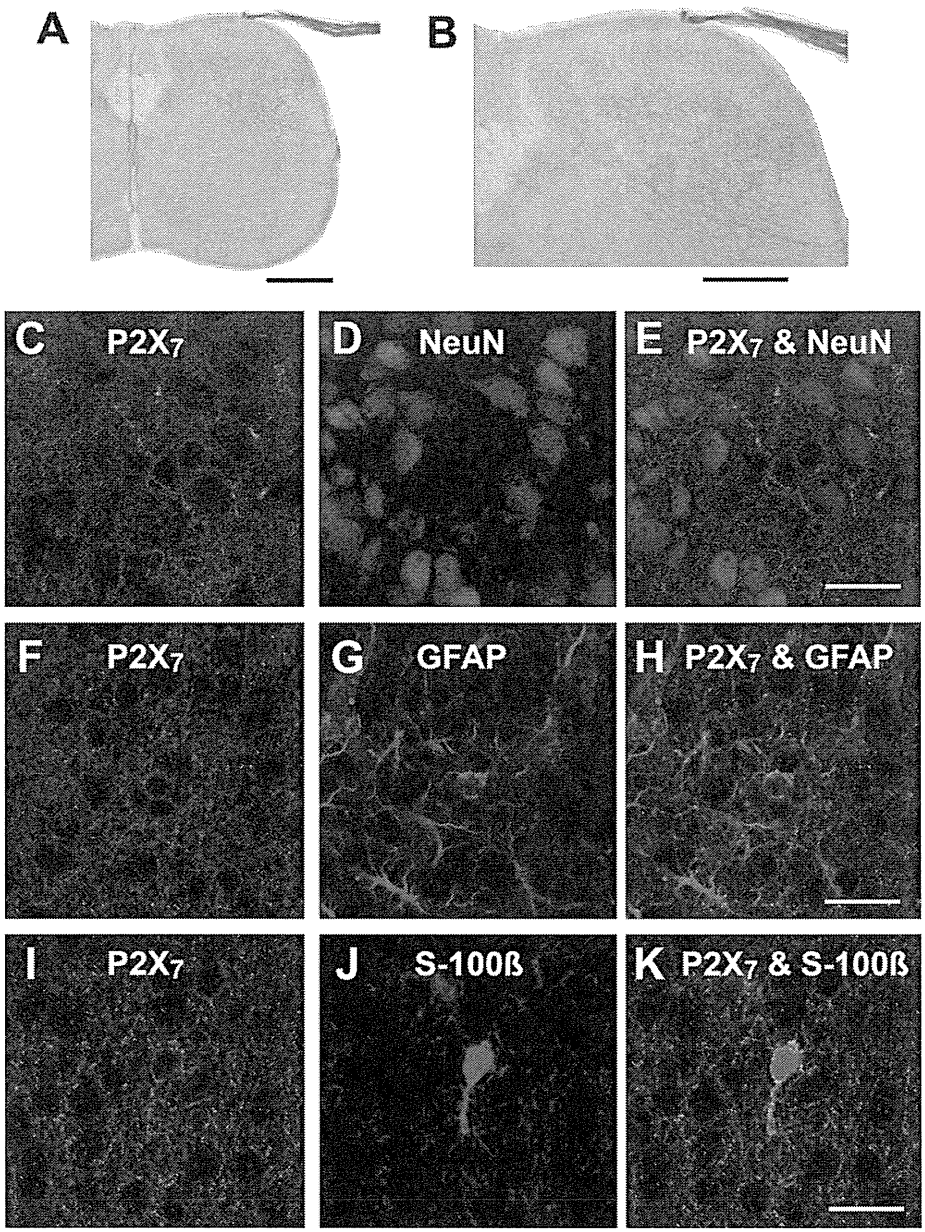

Fig. 10. Distributions of immunoreactivity for $P2X_7$ subunit in the spinal cord. Immunoreactivity for $P2X_7$ subunit is shown as green, and that for neuron-specific nuclei N (NeuN), glial fibrillary acidic protein (GFAP), and S-100-protein β-subunit (S-100β) is shown as red. For details, see the text. Bar in panel A: 300 μm. Bar in panel B: 200 μm. Bar in panels E, H, and K: 20 μm.

P2X receptors enhance synaptic glutamate release when the dorsal roots are stimulated again, and the released glutamate activates and depolarizes not only postsynaptic neurons but also the neighboring astrocytes, similarly as reported by voltage imaging with preferential staining of glial cells in the hippocampus [39,42]. Our voltage imaging data suggest that P2X receptor-mediated potentiation of sensory information processing occurs not only in the superficial layer but more importantly in the deep layer. Earlier reports on the excitatory action of ATP on the signal processing in the dorsal horn [4,23,45,46] are worthy to be reinterpreted from the viewpoint that extracellularly applied ATP potentiates synaptic transmission by activating presynaptic, postsynaptic, and astrocytic P2X receptors.

In addition, our observation that, at lower temperature, attenuation of depolarizing signals by ATP was more remarkable and the recovery of depolarizing signals after washout of ATP was weaker, suggests that P2X receptor-mediated excitatory and P1 receptor-mediated inhibitory actions are temperature dependent, especially in the deep layer.

4.3. Functional and anatomical distribution of P2X receptor subunits in dorsal horn

Our experimental findings that αβmeATP, which is a homomeric $P2X_1$, $P2X_3$, and heteromeric $P2X_{2/3}$ and $P2X_{1/5}$ subtypes agonist [43], reproduced the enhancing action of ATP seen after it was washed out and that PPADS, which is a homomeric $P2X_1$, $P2X_2$, $P2X_3$, $P2X_5$, and heteromeric $P2X_{2/3}$ and $P2X_{1/5}$ subtypes antagonist [43,55], suppressed the enhancing action of ATP indicate that $P2X_1$, $P2X_3$, and/or $P2X_5$ subunits are involved in the enhancing action of ATP.

Although there have been a large number of reports on the expression of P2X receptor subunits in the dorsal horn [6,12–14,24,36,44,68,70–72], in the present study we, for the first time,

Table 2
Distributions of immunoreactivity for P2X receptor subunits.

P2X subunit	Distribution	Related figures
$P2X_1$	Densely positive in neuropils in laminae I–II	Fig. 9A–E
$P2X_2$	Weakly positive only in dorsal root fibers	Not shown
$P2X_3$	Positive in dorsal root fibers and in neuropils that surround neurons and astrocytes in the dorsal horn	Fig. 9F–J
$P2X_4$	Positive in small cells in the gracile fasciculus and in the entire dorsal horn. Also positive in dorsal root fibers and in neuropils surrounding neurons	Fig. 9K–O
$P2X_5$	Sparsely positive in fibers in laminae I–III. Also positive in small-sized neuronal cell bodies	Fig. 9P–T
$P2X_6$	Positive in neuropils in the entire gray matter but sparsely positive in laminae I–II	Fig. 9U–Y
$P2X_7$	Strongly positive in dorsal root fibers and in neuropils in the entire dorsal horn. Positive in astrocytes on and around their cell bodies	Fig. 10A–K

conducted systematic analyses of all 7 P2X receptors subunits distribution. On the basis of our immunohistological analysis and those previous reports, the distribution and anatomical organization of P2X receptor subunits that are important in sensory signal processing in the dorsal horn could be described as follows: The $P2X_1$ and $P2X_3$ subunits, expressed presumably at least partly at afferent nerve terminals of dorsal root ganglion neurons, are distributed mainly in the superficial layer surrounding neurons and astrocytes, and are likely involved in formation of neuron–neuron and neuron–astrocyte (ie, tripartite) synapses. On the contrary, the $P2X_6$ subunit that is also expressed presumably, at least partly, at afferent nerve terminals is distributed mainly in the deep layer, and is also likely involved in formation of tripartite synapses. Although there have been few reports on the expression of P2X receptors in astrocytes in the spinal cord, we found that the $P2X_7$ subunit is expressed in astrocytes in the dorsal horn. Our finding is in agreement with the previous studies showing the $P2X_7$ receptor-mediated regulation of glia-specific glutamate aspartate transporter expression in astrocytes [47] and the $P2X_7$ receptor-mediated ATP release from astrocytes [66] in the rat spinal cord.

4.4. Roles of neuron–glia interaction and P2X receptors in sensory information processing

As we demonstrated that $P2X_1$, $P2X_3$, and $P2X_6$ subunits are expressed in neuropils and are distributed in the superficial and deep layers, generally in agreement with previous reports [6,10, 26,53,54,70], these P2X receptor subunits are expressed in presynaptic terminals. In physiological condition, based on our findings and the recent theories of tripartite synapse and gliotransmission, we consider that, when sensory circuitry is once activated, released neurotransmitters, mainly glutamate, activate postsynaptic neurons as well as surrounding astrocytes, and these neurons and astrocytes then release ATP, glutamate, and other mediators [3,19,69]. Thus, released ATP activates other neighboring astrocytes and lets them further release ATP [1,27,61]. Our immunohistochemical analyses suggest that purinergic signaling is mediated to astrocytes likely through $P2X_7$ receptors. As we have shown that activation of P2X receptors augments the slow component of depolarizing optical signals, extracellularly released ATP activates presynaptic terminals and enhances synaptic transmission when next afferent signals reach synapses [26,53]. Further, extracellularly released ATP will act directly on P2X receptors of postsynaptic neurons and augment signal transduction [11,63]. The post-ATP rebound potentiation described in the present study might have resulted from such mechanisms involving P2X receptors. Activation of postsynaptic neurons by ATP is supported by our immunohistological observation that the $P2X_5$ subunit is expressed in neurons, especially in laminae I–III. Although not analyzed in the present study, we must mention that metabotropic P2Y receptors are also expressed in neurons and astrocytes and are likely involved in sensory information processing in the dorsal horn [16,41,76].

Our findings that fluoroacetate suppressed the post-ATP rebound potentiation more prominently in the superficial layer than in the deep layer, and that the density of astrocytes in the dorsal horn was higher in the superficial layer than in the deep layer, suggest that astrocytes play a role in the P2X-mediated modulation of sensory signaling more importantly in the superficial layer than in the deep region. Studies with P2X receptor subtype specific agonists and antagonists in voltage imaging experiments will provide further detailed information on the P2X receptor-mediated neuronal and glial processing of sensory signals in the dorsal horn, and should be conducted in the future.

Although we focused on neurons and astrocytes in the present study, other types of cells are also involved in purinergic sensory information processing in the dorsal horn, for example, microglia through $P2X_4$ and $P2X_7$ subunits [12,13,24,31,68] and possibly oligodendrocytes, as well as their precursor NG-2 glia [18,28].

4.5. Conclusion

Our results indicate that extracellular ATP acts on presynaptic P2X receptors and on postsynaptic neurons and induces larger and longer-lasting excitation of sensory processing circuitry in the superficial layer and more prominently in the deep layer. Astrocytes are involved in this augmentation of sensory information processing, especially in the superficial layer, likely through $P2X_7$ receptor. Extracellularly released ATP in the dorsal horn plays important roles, not only in neuron-neuron, but in neuron–astrocyte, as well as in astrocyte–astrocyte interaction. Our observation suggests that adenosine degraded from ATP prevents overexcitation of the network, ATP induces sensitization of the nociceptive neuron–glia network, and thus they together modulate the sensitivity and threshold of nociception to the optimal level. The present study will be the basis to develop analgesic drugs targeting astrocytes and tripartite synapses. Complex cross-talk among neurons and astrocytes through purinergic signaling could be a common and fundamental mechanism in the information processing in various circuitries in the central nervous system.

Conflict of interest statement

The authors claim no conflict of interest.

Acknowledgements

This work was supported by the Grant-in-Aid for Scientific Research from the Japan Society for Promotion of Science to YO (15590190 and 20590218) and the Keio Gijuku Academic Development Funds to YO.

References

[1] Anderson CM, Bergher JP, Swanson RA. ATP-induced ATP release from astrocytes. J Neurochem 2004;88:246–56.
[2] Aoyama R, Okada Y, Fukuda K, Yoshida H, Nakamura M, Chiba K, Toyama Y. Effect of extracellular ATP on the neuronal network function of the rat spinal cord dorsal horn. Neurosci Res 2004;50:64.
[3] Bardoni R, Ghirri A, Zonta M, Betelli C, Vitale G, Ruggieri V, Sandrini M, Carmignoto G. Glutamate-mediated astrocyte-to-neuron signalling in the rat dorsal horn. J Physiol 2010;588:831–46.
[4] Bardoni R, Goldstein PA, Lee CJ, Gu JG, MacDermott AB. ATP P2X receptors mediate fast synaptic transmission in the dorsal horn of the rat spinal cord. J Neurosci 1997;17:5297–304.